ORNL/TM--9153

DE85 001692

Engineering Physics and Mathematics Division

HADRON-LEPTON CASCADE CALCULATIONS (1-20 GeV) FOR A Pb-Al-LUCITE CALORIMETER*

F. S. Alsmiller
T. A. Gabriel
R. G. Alsmiller, Jr.

*Submitted for Journal publication

Date of Issue: August 1984

Research sponsored by
U.S. DOE Office of
High Energy and Nuclear Physics

Prepared by the
Oak Ridge National Laboratory
Oak Ridge, Tennessee 37831
operated by
Martin Marietta Energy Systems, Inc.
for the
U.S. DEPARTMENT OF ENERGY
under Contract No. DE-AC05-840R21400

TABLE OF CONTENTS

HADRON-LEPTON CASCADE CALCULATIONS (1-20 GeV) FOR A Pb-Al-LUCITE CALORIMETER*

F. S. Alsmiller, T. A. Gabriel, and R. G. Alsmiller, Jr.
Oak Ridge National Laboratory, P.O. Box X, Oak Ridge, TN 37831, U.S.A.

Abstract

The results of Monte Carlo calculations for π^- (1- to 20-GeV) and e^- (1- to 10-GeV) normally incident on the center of a cylindrical calorimeter are presented. The calorimeter design has 60 unit cells of alternating Pb-Al-Lucite plates and is a simplified model of one to be used at the Stanford Linear Accelerator Center. General characteristics of the total and spatial energy deposition are given. Pulse height spectra, as well as spectra of the transverse fractional energy distributions and of their first and second moments, are given to aid in hadron-lepton discrimination. Sampling fluctuations are also examined for this purpose. Some results for the effects of a uniform probability of incidence over the central transverse strip and also some longitudinal discriminants are presented.

I. INTRODUCTION

Calorimeters are an important tool in high-energy experimental physics, and particle discrimination is an important aspect of the use of such devices.[1] Because of the diversity of calorimeter designs and of the experimental situations in which a particular calorimeter is used, there is unfortunately no single method (or group of methods) of particle discrimination that is generally applicable. Much previous work has emphasized longitudinal discriminants.[1,2,3]

In this paper calculated results for incident π^- (1- to 20-GeV) and e^- (1- to 10-GeV) on a particular calorimeter are presented. The calculational procedure and nuclear data used in obtaining these results are similar to those used in the past[4,5] and results similar to those given here have previously been verified by comparisons with a variety of experimental data.[6,7,8,9]

The calorimeter considered here is cylindrical in shape and is composed of a series of Pb-Al-Lucite plates. It is thick for incident e^- (~20 radiation lengths) and thin for incident π^- (~1.4 to 1.8 collision mean-free paths at the energies of interest here). This calorimeter is described in more detail in Section II and is a simplified model of a calorimeter to be used at the Stanford Linear Accelerator Center. Since longitudinal measurements are not made, the possibilities of hadron-lepton discrimination using lateral distributions are of primary interest. Some longitudinal discriminants are also investigated for their general interest.

General characteristics of the total and spatial energy deposition for the incident particle types and energies are given in Section III, and pulse height spectra are presented in Section IV. Sampling fluctuations and transverse fractional energy distributions and moments are presented and discussed as possible hadron-lepton discriminants in Sections V and VI, respectively. Longitudinal discriminants are given in Section VII.

II. METHOD OF CALCULATION

A. Geometry

The geometry used in the calculations is shown schematically in Fig. 1. The calorimeter is composed of 60 identical cylindrically symmetric unit cells. As indicated in the figure, each of the unit cells is composed of a Pb-Al layer of 0.32131 cm and a lucite layer of 1.27000 cm. The Pb-Al layer is composed of 0.08128 cm of Al, followed by 0.15875 cm of Pb, followed by 0.08128 cm of Al, but for calculational simplicity these layers have been homogenized. A multiplicative factor of 1.053 was applied to all thicknesses to account for air between the constituents. The number densities in Table 1 were then calculated. Finally, an additional multiplicative factor of 1.015 was used to account for the increase in effective thickness by averaging over particle slant angle.* The total length of a unit cell was then 1.701 cm. In Table 1, the densities of the various materials and the number densities used in the calculations are given.

The calorimeter has a radius of 111 cm, but the results that will be presented refer primarily to the central region of the calorimeter that is defined to have a radius of 32.0 cm. That is, the entire calorimeter is included in all transport calculations, but the results, e.g., energy deposition, etc. are given for the central region only. The lucite in the central region of each unit cell is divided into nine broad transverse strips, each having a width of 7.10436 cm, as shown in Fig. 1. Furthermore, the orientation of these strips with respect to the transverse x-axis (see Fig. 1) is varied with depth. The orientation of the strips in the first three unit cells in the calorimeter is shown in Fig. 1 and this pattern is repeated throughout the length of the calorimeter. The unit cells are divided into three sets of 20 interleaved cells, each set having a different orientation with respect to transverse axes. Experimental measurements of light output for a given strip number are assumed to be summed over all 20 cells for a given orientation. (The first orientation includes cells 1, 4, 7, ..., 58, etc.)

*The magnitude of this correction was supplied by D. O. Caldwell, University of California at Santa Barbara.

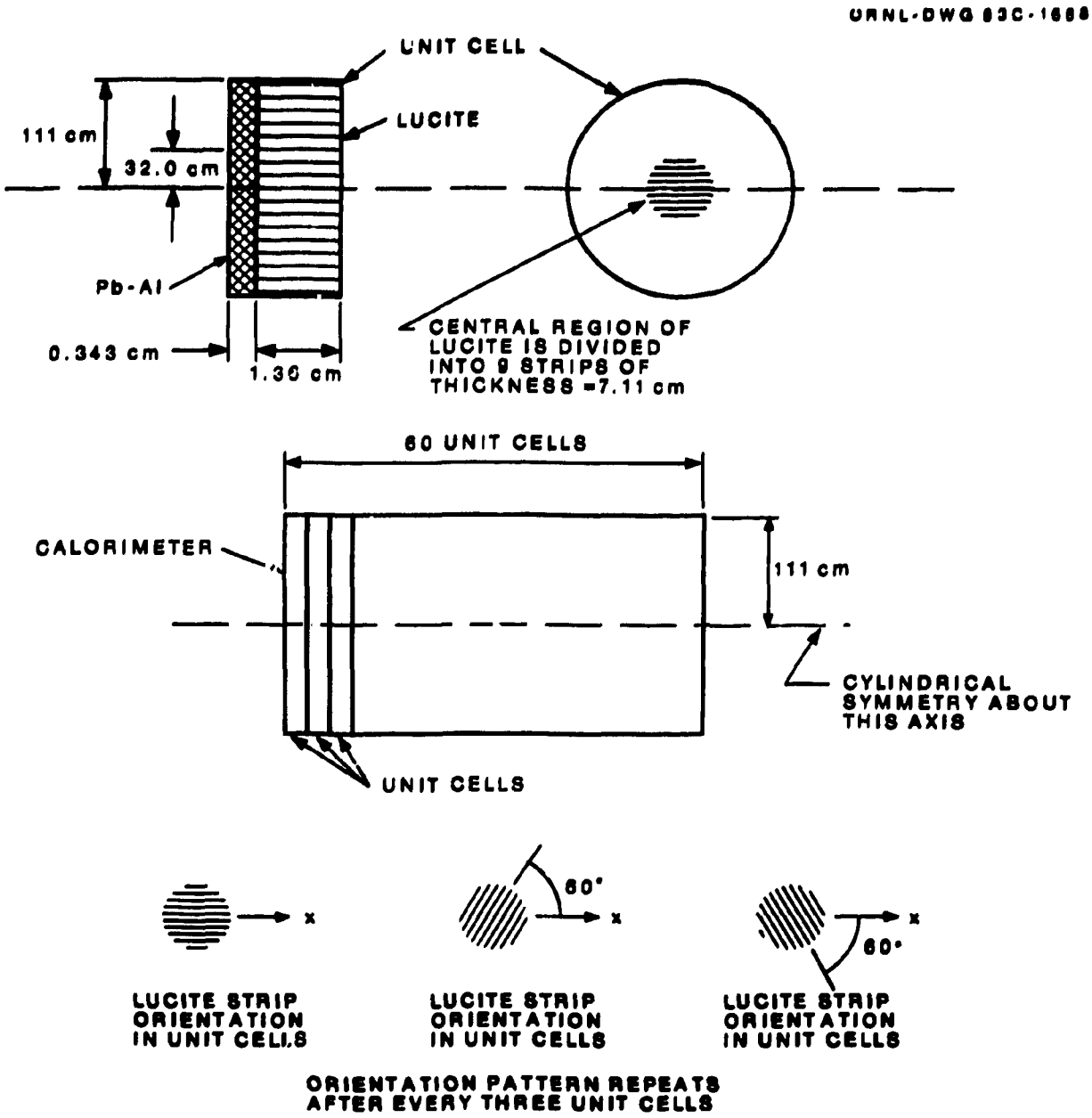

Fig. 1. Schematic diagram of calorimeter.

Table 1

Densities Used in the Calculation

Material	Density ($g\ cm^{-3}$)	
Al	2.70	
Pb	11.34	
Lucite ($C_5 H_8 O_2$)	1.18	
Number Densities (cm^{-3})		
$n_{Al} = 0.0289 \cdot 10^{24}$		homogenized Pb-Al-region
$n_{Pb} = 0.0155 \cdot 10^{24}$		
$n_H = 0.0540 \cdot 10^{24}$		lucite region
$n_C = 0.0337 \cdot 10^{24}$		
$n_O = 0.0135 \cdot 10^{24}$		

B. Cascade Calculations

The π^- induced nucleon-meson cascade calculations were carried out with the three-dimensional multi-media high-energy transport code HETC.[4] This code has been described in detail previously[4,5,6] and has been used in a variety of calorimeter calculations,[6,7,8,9,10] so only a brief discussion will be given here. Calculated results obtained with HETC have been compared with a variety of experimental data, and, in general, good agreement has been obtained.[5,7,9,10,11]

In the HETC code, Monte Carlo methods are used to obtain a detailed description of the particles - nucleons and pions - in cascades induced in the calorimeters by incident pions and nucleons. In HETC, account is taken of the slowing down of charged particles via the continuous slowing-down approximation; nonelastic nucleon-nucleus and charged-pion-nucleus (excluding hydrogen) collisions are treated by the intermediate energy intranuclear-cascade-evaporation model for $E \leq 3$ GeV, and, at energies ≥ 3 GeV, through the use of a scaling model.[5] Elastic (at all energies) and nonelastic (≥ 3 GeV) collisions of nucleons and charged pions with hydrogen are treated by using experimental data;[12] below 3 GeV, nonelastic collisions are described by means of an isobar model.[13]

HETC does not transport photons, produced by π^0 decay and nuclear deexcitation, but provides a source of these photons as a function of energy, angle, and position, so they may be transported by means of an electron-photon cascade code.

In the work reported here, all electron-photon cascade calculations, i.e., the cascade induced by photons produced in HETC and the cascade produced by incident e^-, were carried out using the Electromagnetic Cascade Shower (EGS) code written by Ford and Nelson.[14] This code has been compared with a variety of experimental data and, in general, good results have been obtained.

The Monte Carlo particle histories were analyzed using the CALOR system.[6] This is a collection of analysis routines that were specifically designed to be used with HETC and with an electron-photon cascade code such as EGS to provide quantities of interest in evaluating and analyzing various types of calorimeters. In particular, in this code system, the nonlinearity of the light pulse from a scintillator (i.e., the light output is not proportional to the energy deposition) is taken into account using Birk's Law[6] and this feature has been used in obtaining all of the results presented in the next sections of this paper.

III. GENERAL CHARACTERISTICS OF ENERGY DEPOSITION

The energy deposition by incident pions of kinetic energy E_o that do not undergo a nuclear collision of some kind, somewhere in the entire calorimeter, has been omitted in all figures shown in this and subsequent sections. Approximately 13-17% of all primary pions are of this type, i.e., undergo only ionization energy loss (with straggling); the nonlinear energy deposited in the 60 lucite plates by each such pion is shown in Table 2, as well as the percent number of histories and the number of collision mean-free paths estimated from these fractions. Also, the minimum and maximum energy depositions, $E_{D\min}(E_o)$ and $E_{D\max}(E_o)$, found for the colliding pions in the history sets considered, are given. The amount of energy deposited by the straight-through particles is within the spectral limits for the colliding particles; it should be deposited within the central broad strip determined by the point of impact.

The average effective (nonlinear) energy deposition, $\overline{E}_D$, by the colliding (or contributing) histories in all 60 lucite plates and in all nine broad lateral strips of the calorimeter core is shown as a function of E_o in Fig. 2. Also shown are the maximum and minimum energy depositions, $E_{D\max}(E_o)$ and $E_{D\min}(E_o)$, (dotted lines for each kind of particle) and the standard deviations. The maximum is nearly the same for pions as for electrons, but the pion minimum is very small.

A given energy deposition, E_D, can be produced by a particle with any initial energy between certain limits, $E_{o\min}(E_D)$ and $E_{o\max}(E_D)$, for e^- or π^-. These limits can be read directly from the graph as the values of E_o for which the functions given by the dotted lines, $E_{D\max}(E_o)$ and $E_{D\min}(E_o)$, respectively, equal the specified value of E_D. It is evident that virtually any pion with incident energy greater than the required minimum for an electron could

Table 2

Average Nonlinear Energy Deposition for Noncolliding π^- and Maximum and Minimum Energy Deposition for Colliding π^-

E_0 (GeV)	% st thru	$\bar{E}_{D,\text{st thru}}$ (MeV)	No. of Coll. mfp	$E_{D\min}(E_0)$ (MeV)	$E_{D\max}(E_0)$ (MeV)
1.0	12.7	186 ± 0.7	1.36	17.3	495
2.5	15.2	196 ± 0.8	1.65	29.3	1049
5.0	17.2	208 ± 1.1	1.84	206	1967
10.0	15.6	222 ± 4.4	1.70	221	3835
20.0	16.5	247 ± 5.5	1.80	236	7504

produce any energy deposition greater than 500 MeV, with some probability. Hence, energy deposition alone is not a hadron-lepton discriminant.

Even if E_0 (or the initial momentum) is measured in advance, it is difficult to completely discriminate lower energy hadrons from leptons on the basis of total energy deposition. The subsets of pions depositing energy within the electron $E_{D\min}$ and $E_{D\max}$ limits for the same E_0 are treated separately in this paper. Since these are only 1.1% of the number of colliding histories at 10 GeV, 3.1% at 5 GeV, 9% at 2.5 GeV, and 41% at 1 GeV, the statistics are very poor and errors are not always given.

The resolutions $\sigma_{ED}/\bar{E}_D$ calculated from the error bars in Fig. 2 are shown in Fig. 3. These resolutions, especially for the 10-GeV electrons, are probably smaller than can be obtained experimentally, since light collection statistics, noise, etc., are not included in these calculations. Energy spectra are shown in the next section.

The longitudinal distribution of energy deposited in each lucite plate (integrated laterally) is shown in Fig. 4 as a function of plate number. The standard deviations can be found for each plate by multiplying the statistical errors in the average shown by approximately 30. The large standard deviations indicate that the unique patterns of longitudinal distribution shown need not hold for individual events; these may vary considerably from the average.

The calorimeter is thick from the point of view of an electron-photon cascade (of the order of 20 radiation lengths), but thin from the point of view of the nucleon-meson cascade, as evidenced by the number of mean-free paths in Table 2. Almost all electrons deposit only a

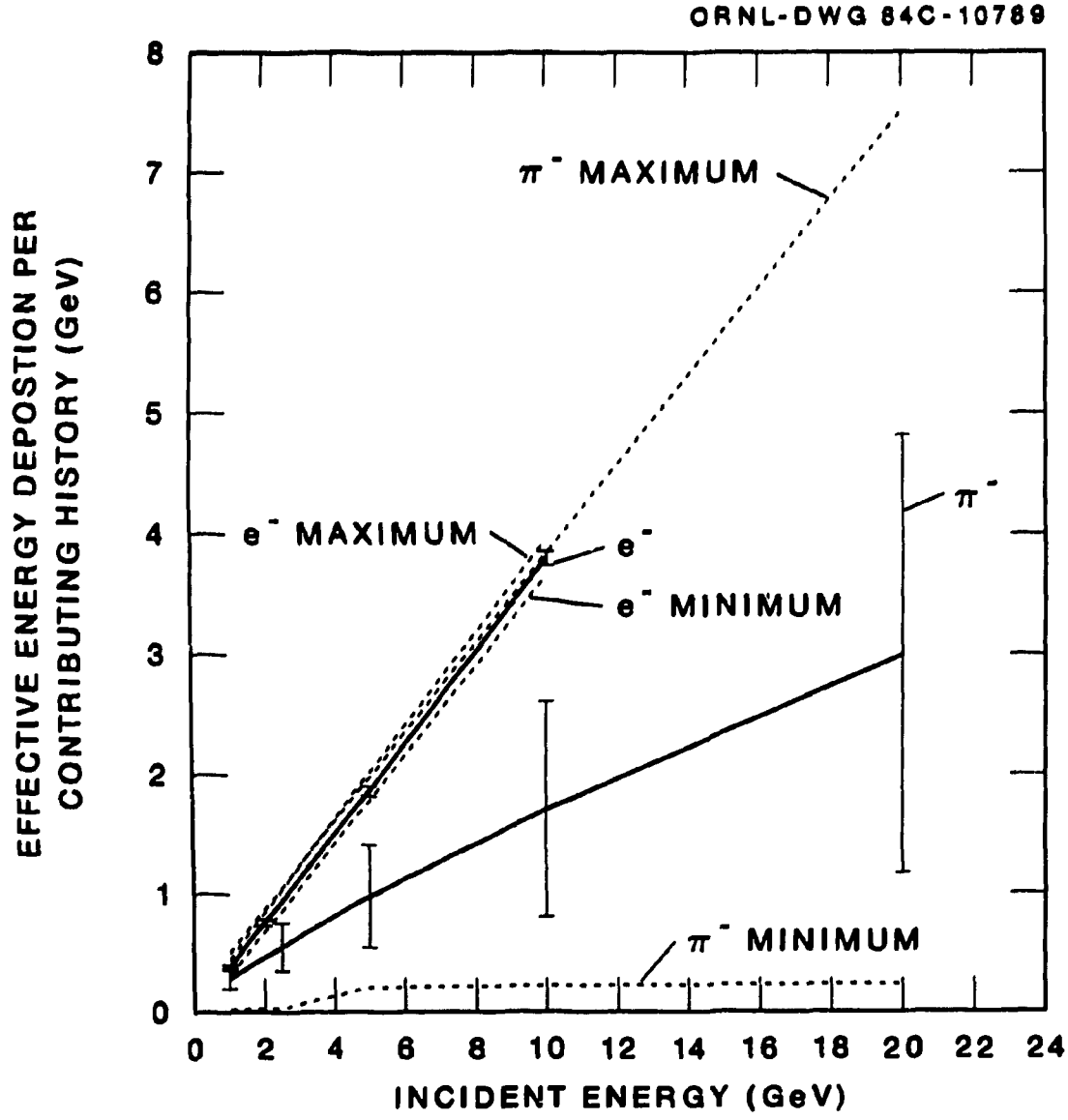

Fig. 2. Effective energy deposition per contributing history vs. incident energy for incident e^- and π^-. The error bars represent the standard deviation of the energy deposition distributions. The dotted lines represent minimum and maximum energy depositions.

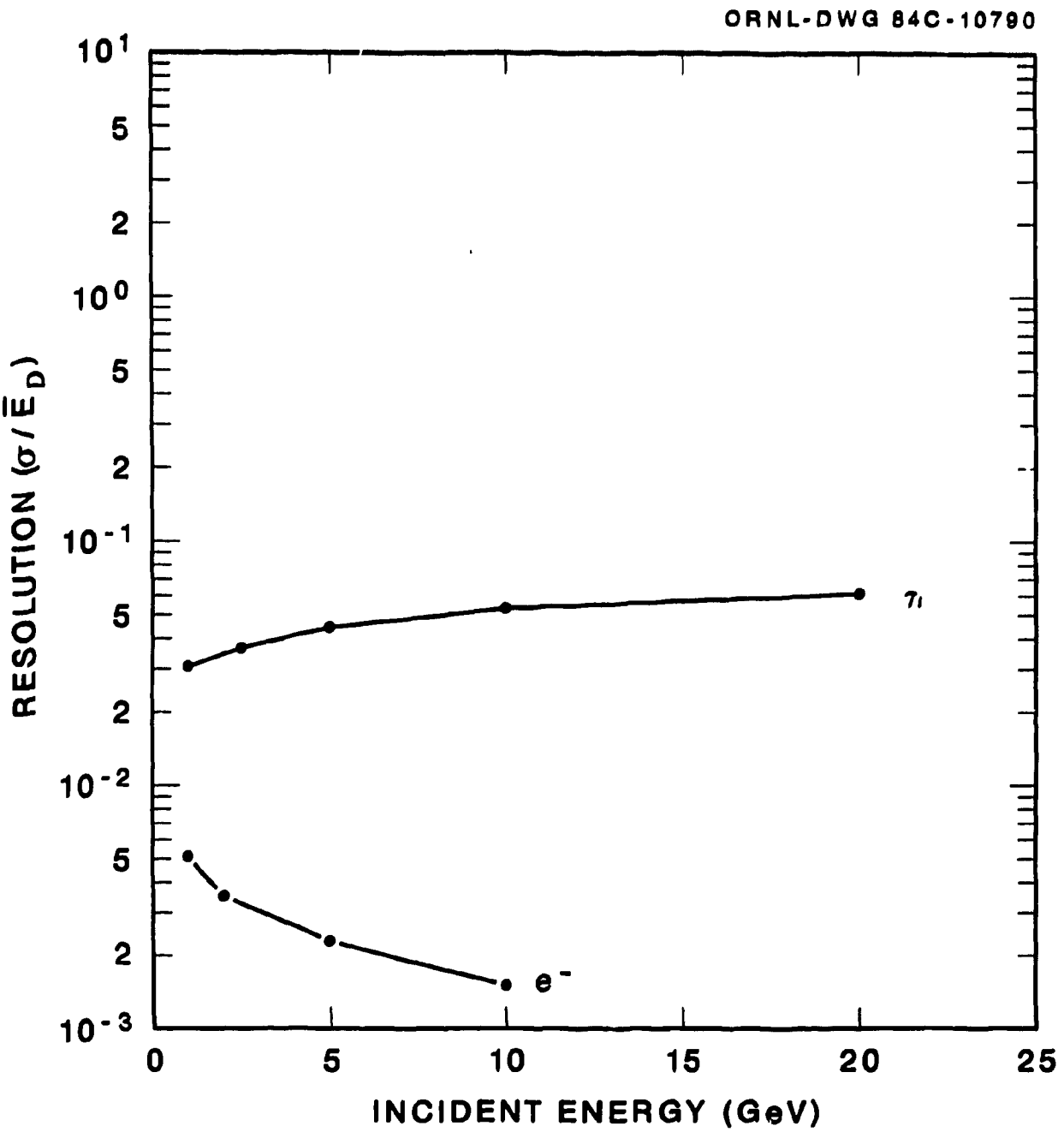

Fig. 3. The ratio of the standard deviation of the effective energy deposition to the effective energy deposition vs. incident energy for incident e^- and π^-.

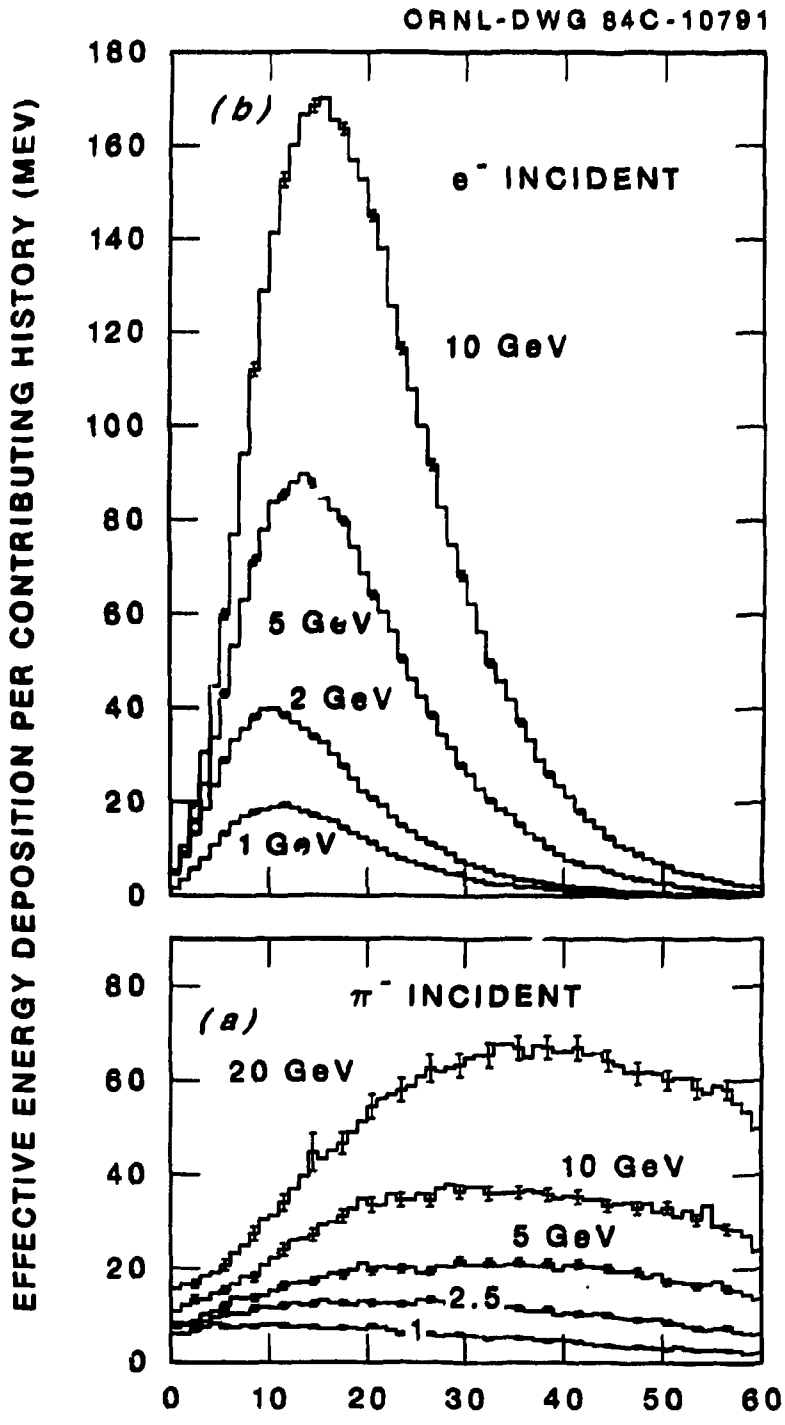

Fig. 4. Effective energy deposition per contributing history in each lucite plate vs. lucite plate number (see Fig. 1) for incident a) π^- and b) e^-. The error bars represent the statistical error.

negligibly small amount of energy (<8 MeV)* in the back lucite plate of the calorimeter. For pions, particularly at the higher incident energies, the cascade (on the average) takes a longer distance to develop because primary particles suffer only dE/dX losses until the first collision, which may occur relatively late, and because the secondary particles generally are more numerous, more energetic, and more forward as E_0 increases. Hence, as E_0 increases from 1 to 20 GeV, from 6% to 81% of the pion cascades will deposit more than 8 MeV in plate 60. Measurements in this plate alone (or in several plates at the back) might be a good discriminant for high energy pions with $E_0 > 5$ GeV (see Section VII).

Also shown in Fig. 4c are the longitudinal distributions of energy for the subset of high-energy-deposition pions with $E_{Dmin,e^-}(E_0) \leq E_D \leq E_{Dmax,e^-}(E_0)$, i.e., those π^- that can be confused with e^- when a prior determination of initial energy is made in addition to the total energy deposition. It is evident that these high-energy depositions result in rather flat longitudinal π^- distributions that look very much like the complete π^- distributions at E_0 of 2.5 GeV or less, but peak in the left half of the calorimeter at $E_0 \geq 5$ GeV, as do e^-.

Finally, for 10-GeV e^- and 10-GeV π^-, the lateral distributions of nonlinear energy deposition, summed over all 60 lucite plates, are shown in Fig. 5a, as a function of fine strip width (six fine strips of width y = 1.18406 cm are included in one broad strip). For a given energy, E_0, the electron lateral spreading is not as great as for pions, with a greater deposition in the center. In Fig. 5b, the total 10-GeV π^- energy distribution is shown broken up into the hadronic and electron-photon components, respectively. The distributions are nonuniform in transverse distance, y, and are not Gaussian in energy (except for the three center broad strips).

Experimental measurements are assumed to be for the broad strips only and will include the effects of the primary particle having an essentially uniform probability of incidence at any point, y_0, in the broad strip first entered, strip 5. The computed average effective energy deposited in each broad strip, $\bar{E}_{Dj}$, j = 1,9, averaged over the points of incidence, is shown in Fig. 6a for e^- and Fig. 7a for π^-. Estimated resolutions are given in Figs. 6b and 7b.

The pattern of experimental $\bar{E}_{Dj}$ values for an individual particle may be asymmetrical for several reasons: 1) the cascade may develop asymmetrically; 2) the particle may enter "strip 5" off-center, i.e., $-3\Delta y \leq y_0 \leq 3\Delta y$; and 3) the identification of "strip 5" experimentally may be doubtful, for pions at least, if it depends on the assumption that the energy or the fraction of energy deposited in that strip is a maximum. Typical spectra of energy fractions for some strips are shown in Section V; they will be broadened if averaged over y_0.

*At 10 GeV, 5% of the electrons deposit more than 8 MeV in plate 60.

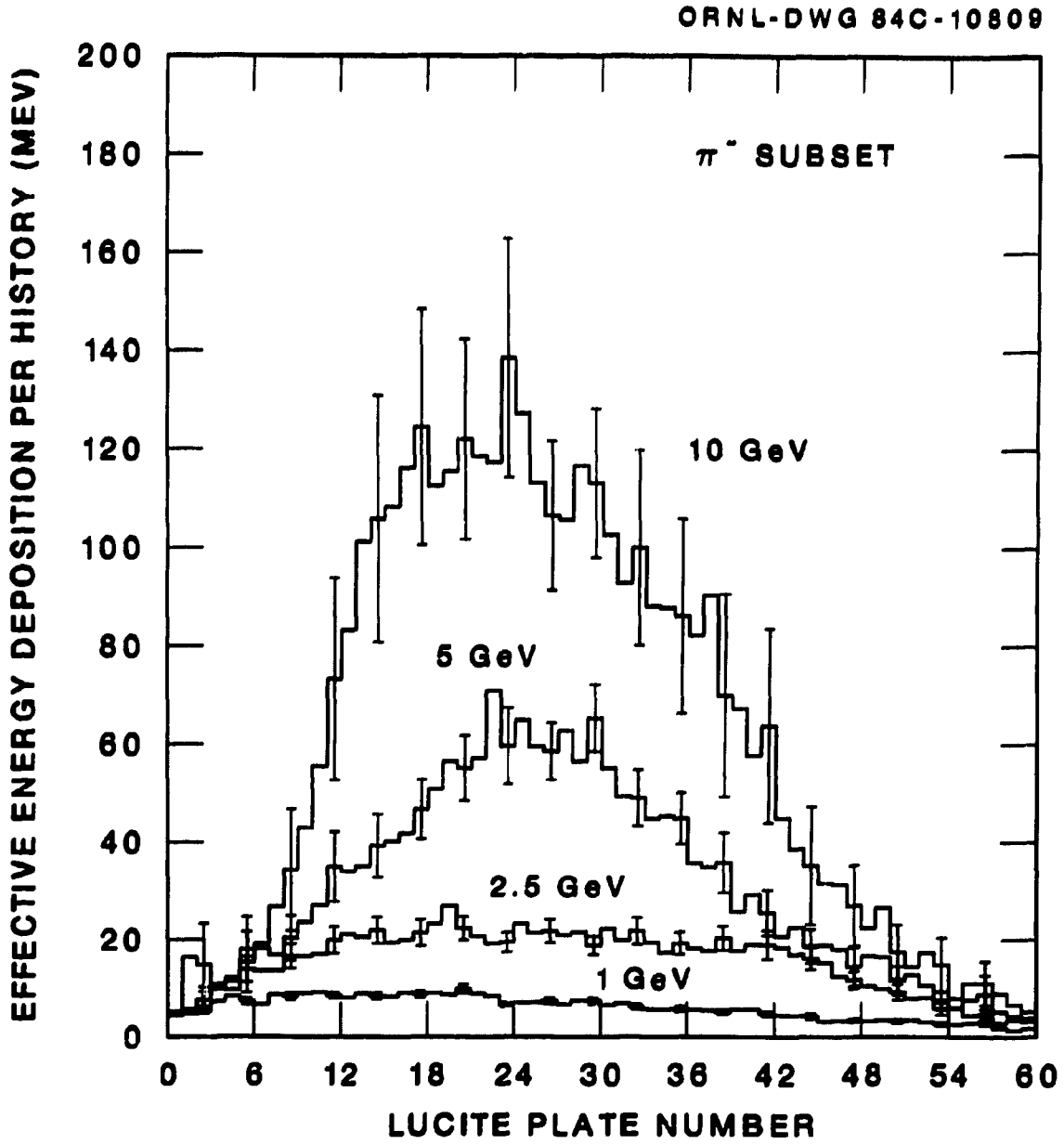

Fig. 4c. Effective energy deposition per history in π^- subsets (where π^- deposit energy within the e^- limits) in each lucite plate vs. lucite plate number. The error bars represent the statistical error.

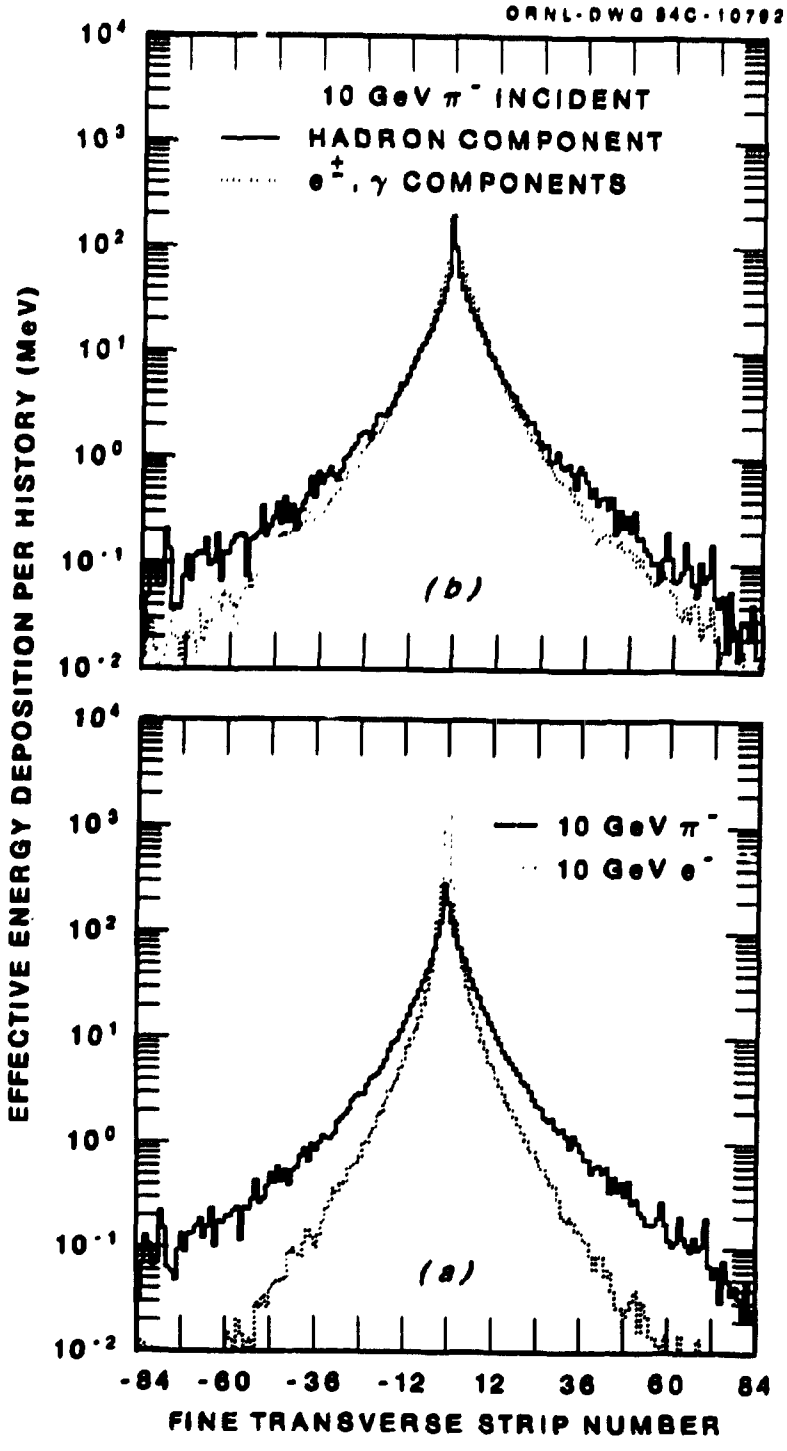

Fig. 5. a) Average transverse effective energy deposition vs. lateral distance from center (fine strip Δy = 1.18046 cm) for 10 GeV incident π^- and e^-; b) hadronic component and electron-photon component of average effective energy deposition vs. lateral distance from center for 10 GeV π^- incident.

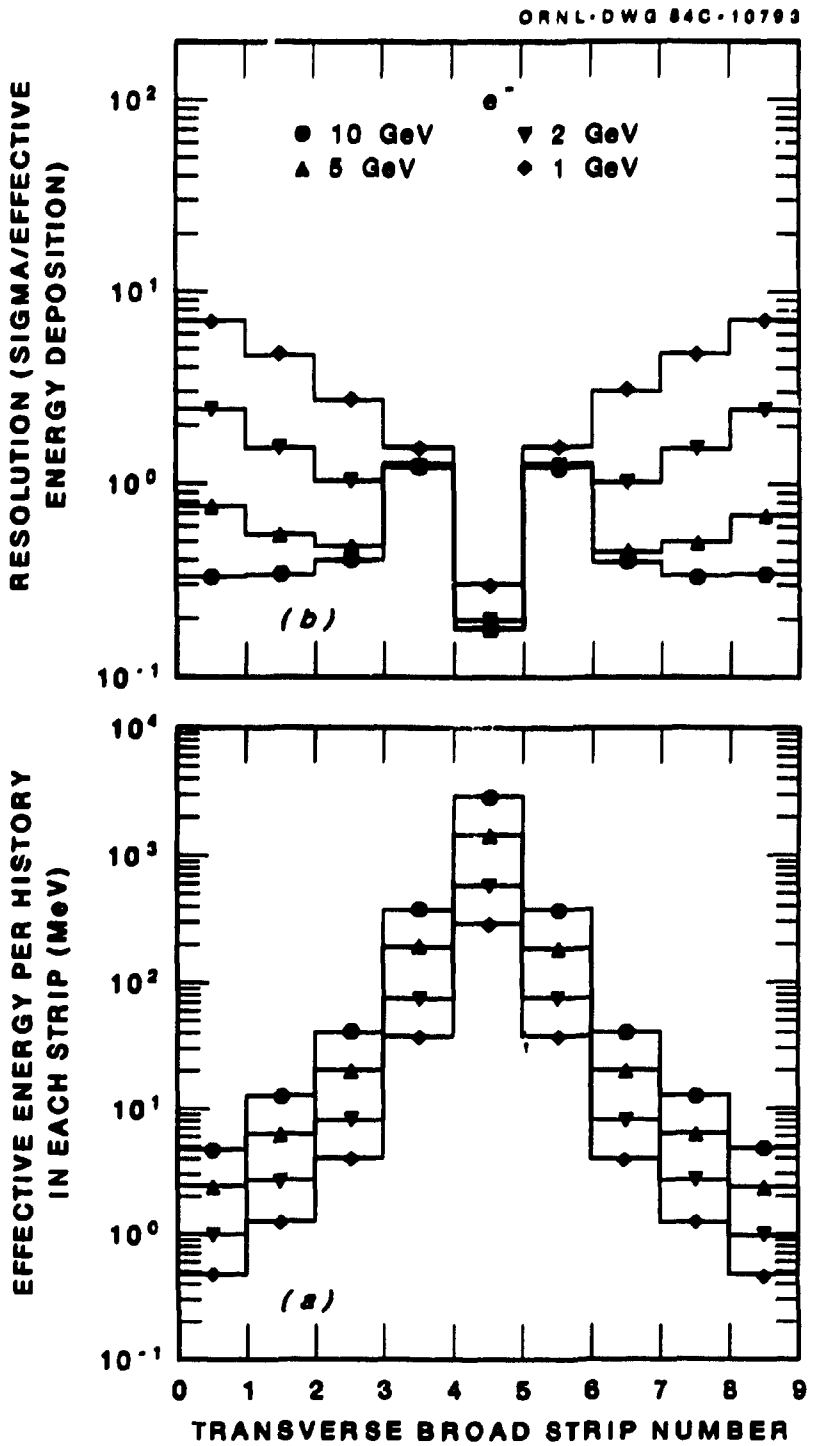

Fig. 6. a) Nonlinear energy deposition, $\overline{E}_{Dj}$, in broad strips, integrated longitudinally for incident e^-; b) resolution, $\sigma_{EDj}/\overline{E}_{Dj}$, for incident e^-.

The first two of the above reasons contribute to large standard deviations for $\bar{E}_{Dj}$; (estimated resolutions $\sigma_{\bar{E}Dj}/\bar{E}_{Dj}$ were shown in Figs. 6b and 7b). Since they are so large, it is difficult to use the lateral energy distributions as discriminants. Other statistics of the lateral distribution are shown in Sections V and VI.

IV. ENERGY SPECTRA

Pulse height distributions for e^- and π^-, summed over all lucite plates and all strips in the core of the calorimeter are shown in Figs. 8 and 9; these are the number of contributing histories in a given interval, ΔE_D, of nonlinear energy deposition.

For electrons, the Gaussians computed with the quoted σ's,

$$\sigma_{ED} = \left[\frac{1}{(N-1)} \sum_{n=1}^{N} (E_{Dn} - \bar{E}_D)^2 \right]^{\prime\prime} \tag{1}$$

where E_{Dn} is the energy deposited by history n, are a very good fit. They have been renormalized by the number of colliding histories, N, and the ΔE_D interval.

For pions, the Gaussian fits are better than might be expected except at the lower energy limits. A substantial number of incident pions interact toward the end of this calorimeter, thereby allowing for greater leakage and smaller pulse height signals.

Table 3 shows the values of $\bar{E}_D/E_0$ for the set of 20 lucite plates in each of the three strip orientations described in Section I. The spectra for each orientation are very similar to those in Figs. 8 and 9.

V. SAMPLING FLUCTUATIONS

A kind of longitudinal fluctuation is shown in Fig. 10, where extrapolated standard deviations of the differences in energy deposition between orientations are shown. The averages are nearly but not quite zero, because the plates of orientations two and three are systematically one and two plates downstream from those of orientation one. They can be obtained by consulting Table 3. Some, but not much, hadron-lepton discrimination appears possible from these difference distributions.

The standard deviations of two transverse sampling fluctuations are shown in Fig. 11. Both have averages nearly zero for both e^- and π^-. The first, a, is for the left-hand side (broad strips 1-4) minus the right-hand side (broad strips 6-9) energy deposition integrated longitudinally, and shows left-right asymmetry to be much larger for many π^- cascades than for most e^- cascades. The second, b, is for the sum of energy deposited in strips 1 + 3 + 6 + 8 minus the sum deposited in strips 2 + 4 + 7 + 9 and shows even more pronounced differences. Particles with either fluctuation energy greater than 50 to 100 MeV, as E_0 increases, are outside two standard deviations for e^-, but inside one standard deviation for π^-. However, the σ's shown will be somewhat broadened if uniform probability of incidence over all points in strip 5 is assumed.

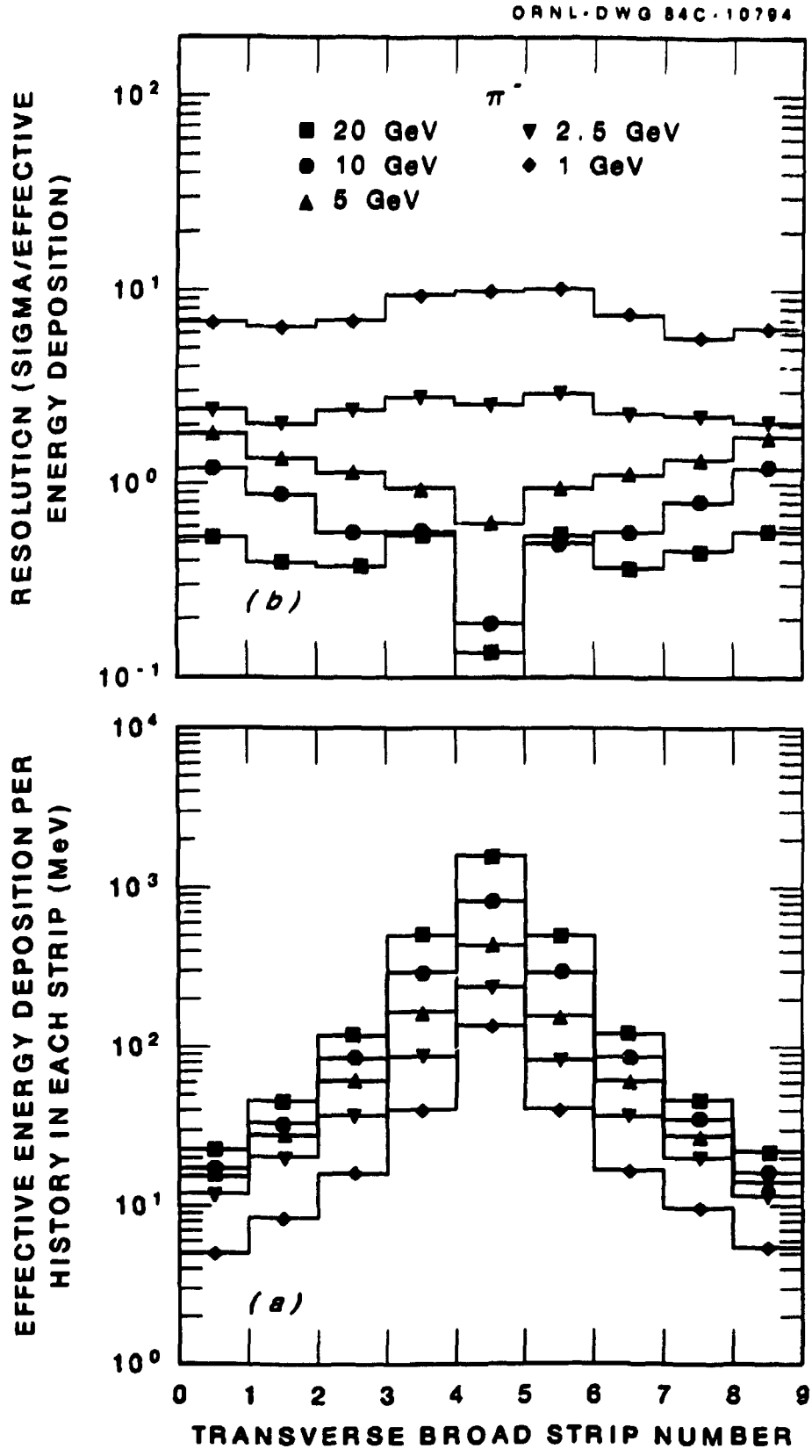

Fig. 7. a) Nonlinear energy deposition, $\overline{E}_{Dj}$, in broad strips, integrated longitudinally for incident π^-; b) resolution, $\sigma_{EDj}/\overline{E}_{Dj}$, for incident π^-.

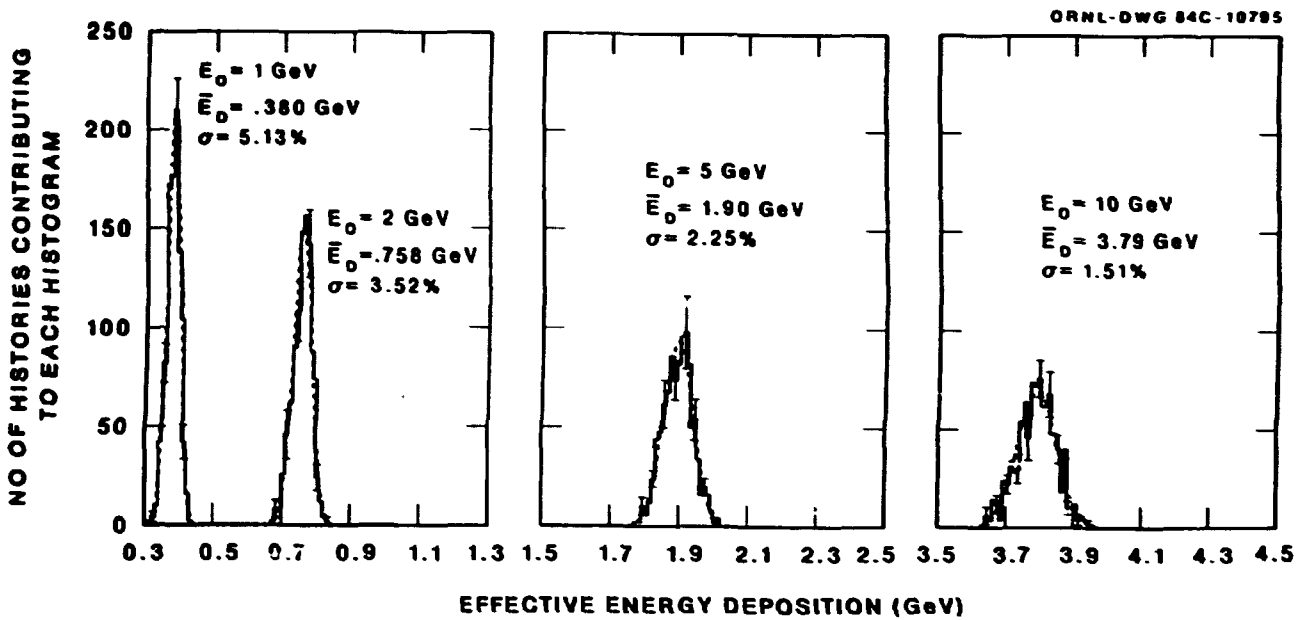

Fig. 8. Effective energy deposition spectra for incident e^-. The sum of the histogram values for a given incident energy is the total number of histories. For each E_0 the Gaussian curve and the histogram are normalized to the same area, i.e., to the product of the histogram energy interval (20 MeV) and the total number of histories (1000).

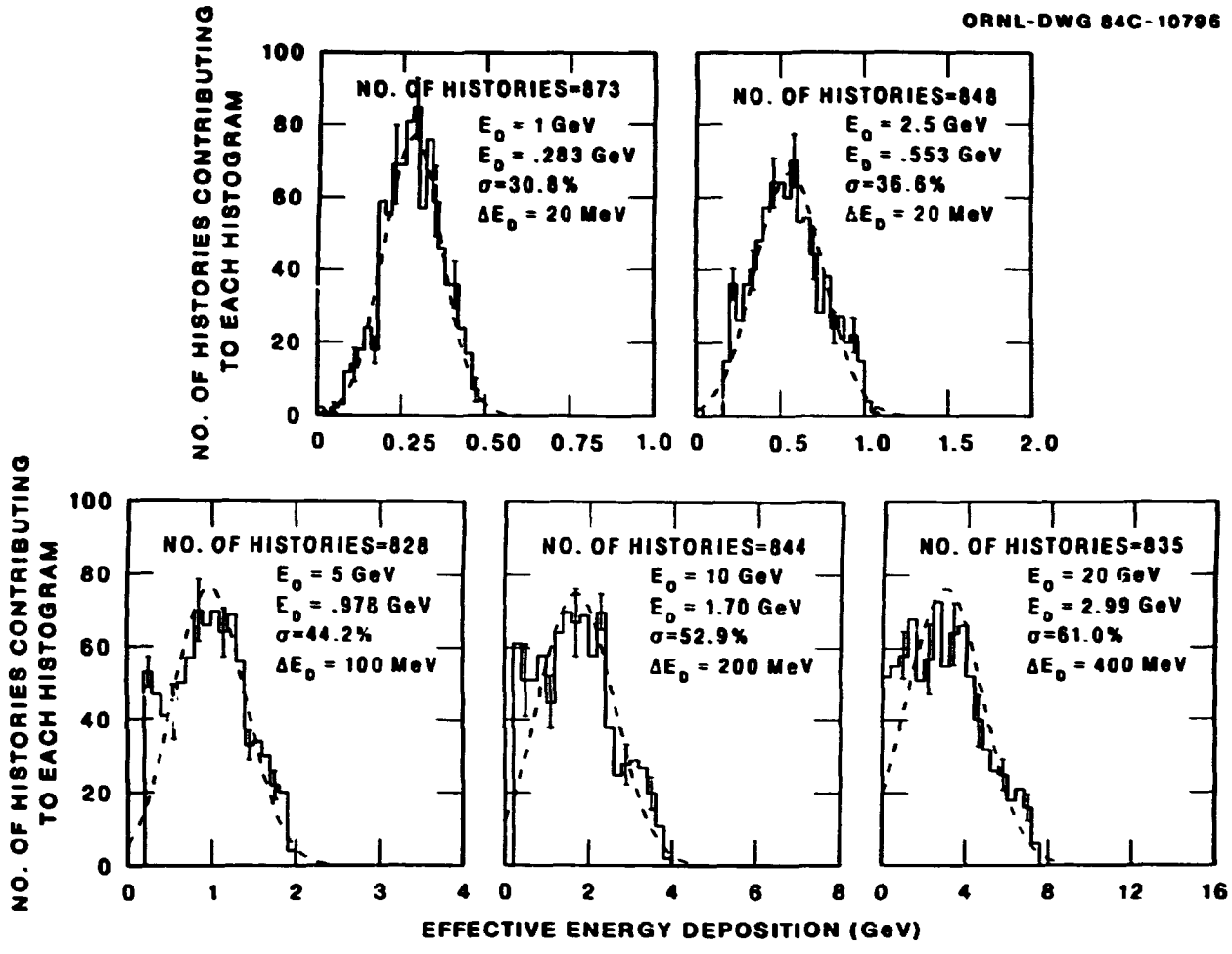

Fig. 9. Effective energy deposition spectra for incident π^-. The sum of the histogram values for a given incident value is the total number of contributing histories. For each E_0 the Gaussian curve and the histogram are normalized to the same area, i.e., to the product of the histogram energy interval and the total number of contributing histories.

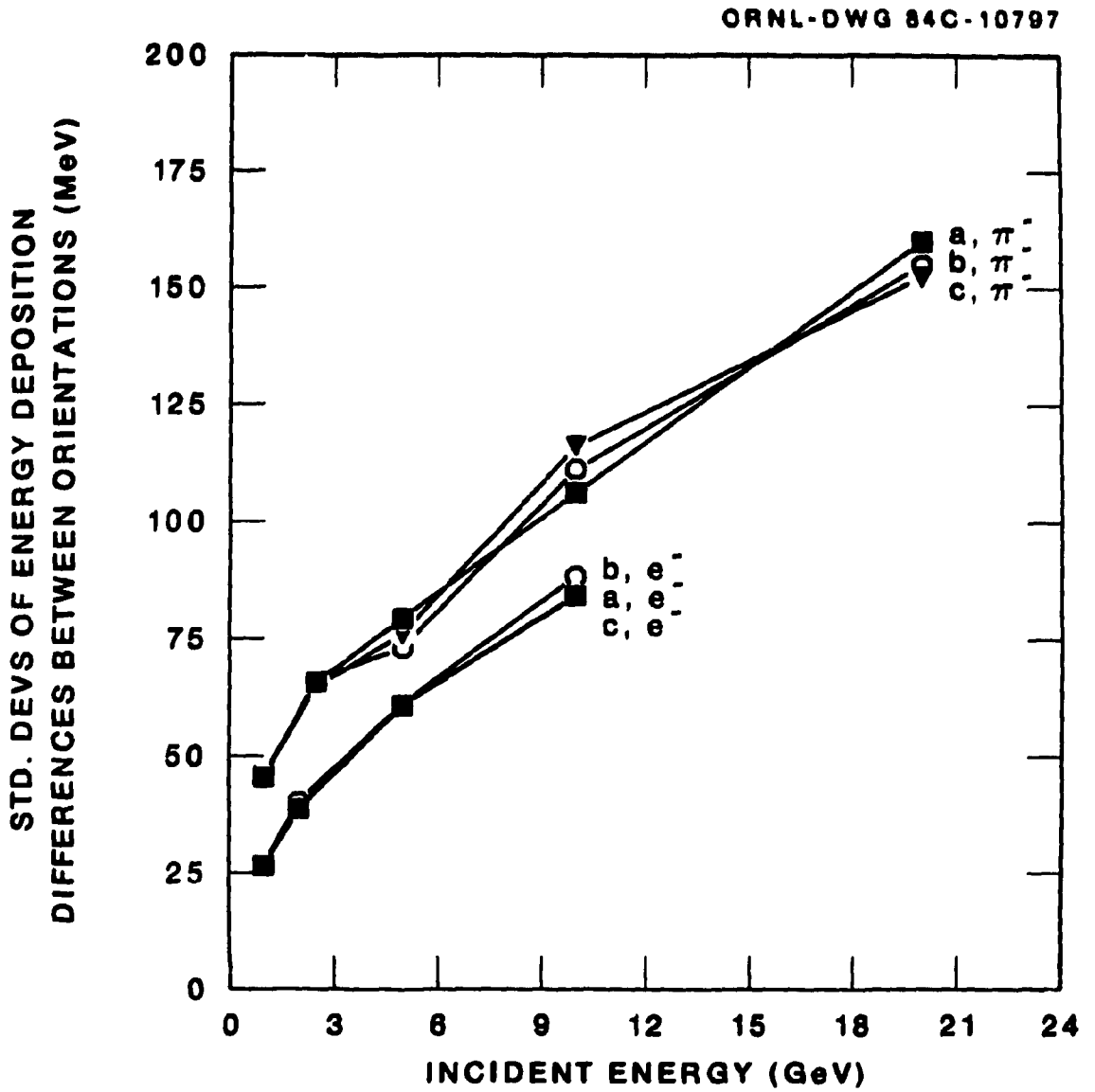

Fig. 10. Standard deviations of the effective energy deposition differences between the lucite plates of different orientations: a) one minus three, b) two minus three, and c) one minus two.

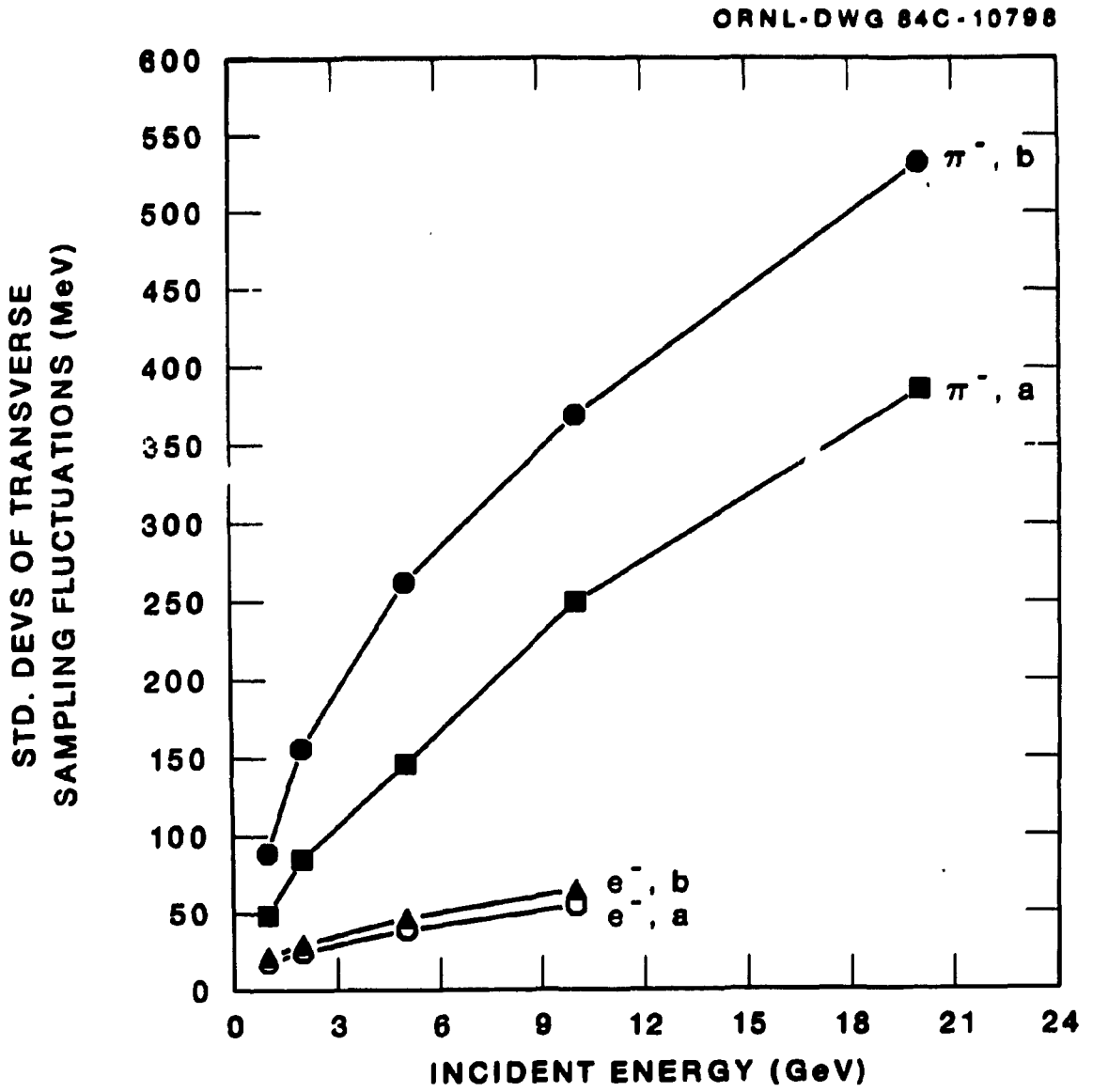

Fig. 11. Standard deviations of the spectra of lateral energy deposition in broad lucite strips: a) 1+2+3+4 minus that in strips 6+7+8+9 summed over all lucite plates for incident e^- and π^-, and b) 1+3+6+8 minus that in strips 2+4+7+9 summed over all lucite plates for incident e^- and π^-.

Table 3

Effective Energy Deposition and Standard Deviation of the Energy Deposition in Lucite Plates of a Given Orientation (see Fig. 1) for Incident e^- and π^-

Note: The energy depositions are divided by E_0 and the standard deviations are divided by the effective energy deposition for a given orientation.

E_0 (GeV)	Orientation 1 $\bar{E}_{D1}/E_0$	Orientation 1 $\sigma_{ED1}/\bar{E}_{D1}$	Orientation 2 $\bar{E}_{D2}/E_0$	Orientation 2 $\sigma_{ED2}/\bar{E}_{D2}$	Orientation 3 $\bar{E}_{D3}/E_0$	Orientation 3 $\sigma_{ED3}/\bar{E}_{D3}$
			Incident e^-			
1.0	0.13	0.13	0.13	0.13	0.13	0.13
2.0	0.13	0.092	0.13	0.10	0.13	0.10
5.0	0.13	0.060	0.13	0.060	0.13	0.060
10.0	0.13	0.040	0.13	0.043	0.13	0.042
			Incident π^-			
1.0	0.095	0.40	0.095	0.41	0.093	0.43
2.5	0.073	0.42	0.074	0.41	0.074	0.43
5.0	0.065	0.47	0.065	0.46	0.065	0.46
10.0	0.056	0.55	0.057	0.54	0.057	0.54
20.0	0.049	0.62	0.050	0.61	0.050	0.62

VI. TRANSVERSE FRACTIONAL ENERGY DISTRIBUTIONS AND MOMENTS

In this section it is important to keep in mind that strip 5 is assumed to be the strip in which impact is first made; results are for center incidence in this strip unless otherwise stated. It is assumed that a total of four broad strips exist on either side of this center strip. In an experimental situation, a particle may be incident to one side of the area designated as the core, so that fewer than nine strips can be used to keep the symmetry. Omission of some strips may not affect the energy fractions unduly, since fractions in the outlying strips are small; however, the first and second moments will be cut down considerably.

Figures 12-14 show the conditional probabilities, $P_c(F_{nj},E_0)$, for energy deposition fractions F_{nj} at fixed incident energy for 5-GeV π^- and e^- in strip 4 (strips 4 and 6 were averaged) and strip 5.

For history n, point of incidence y_0, and strip j,

$$F_{nj}(y_0) = E_{nj}(y_0) / \sum_{j'=1}^{9} E_{nj'}(y_0) \ . \tag{2}$$

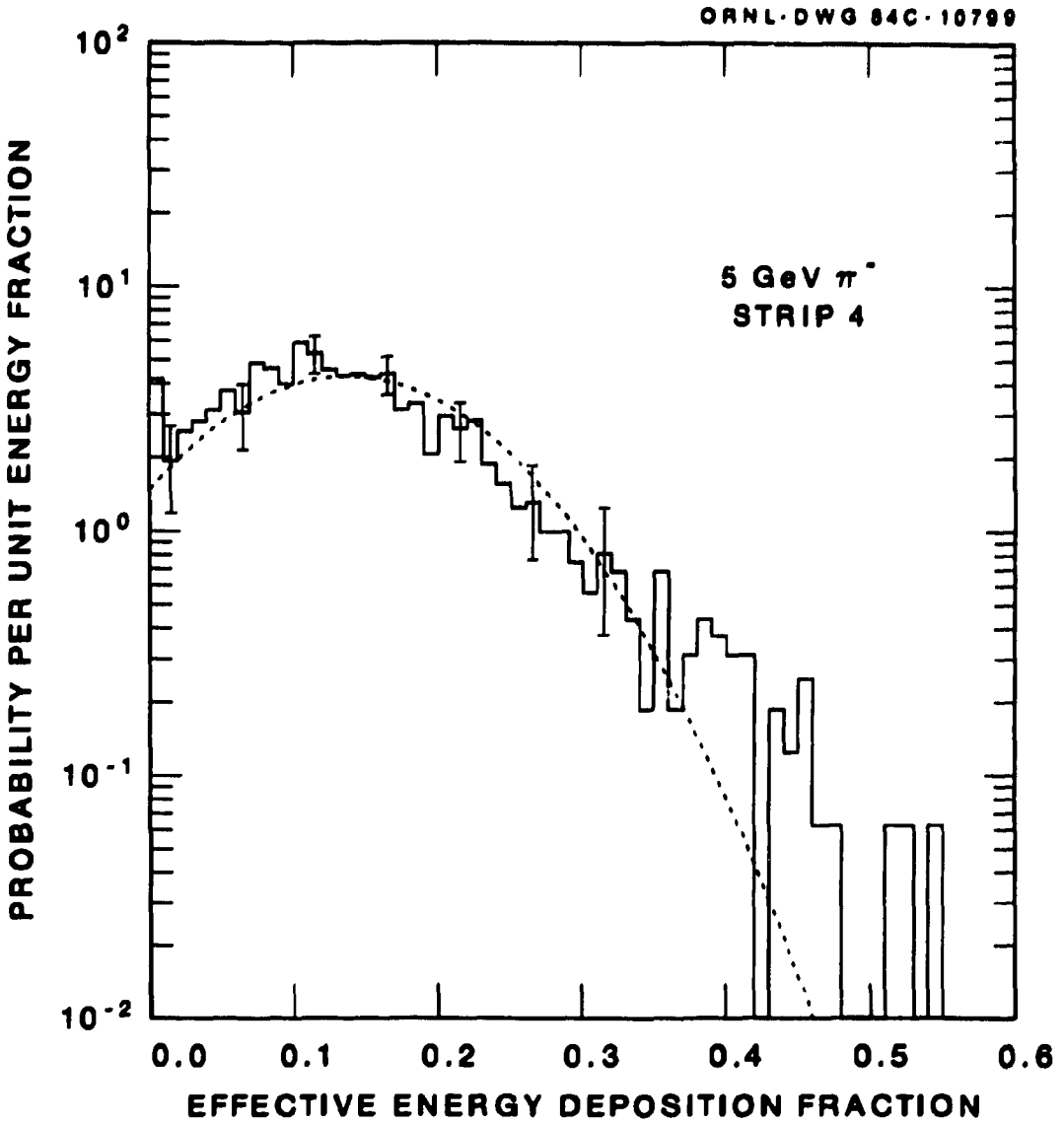

Fig. 12. Probability per unit energy fraction vs. effective energy deposition fraction for broad transverse strip 4 when 5-GeV π^- is incident at the center of strip 5.

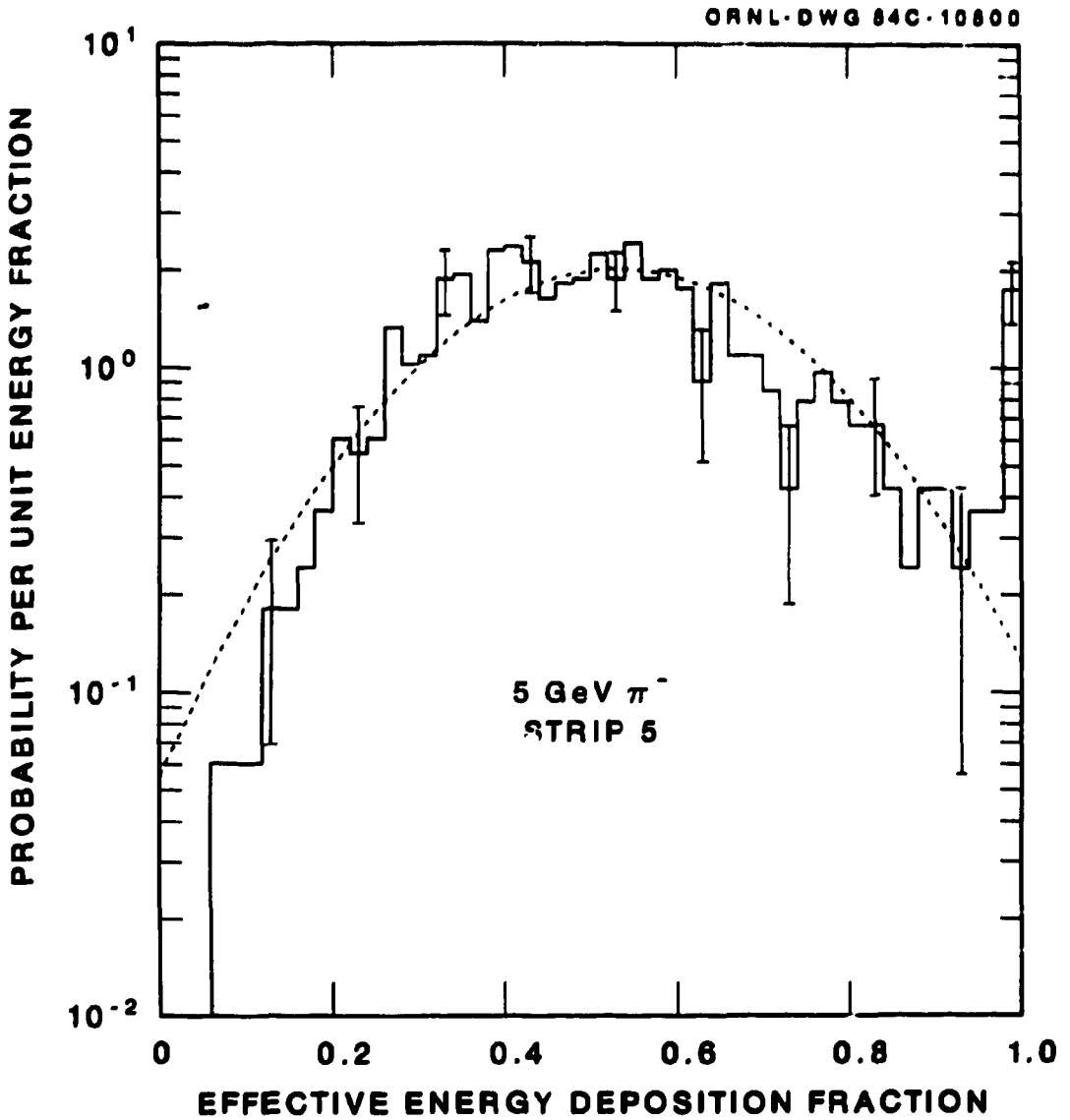

Fig. 13. Probability per unit energy fraction vs. effective energy deposition fraction for broad transverse strip 5 when 5-GeV π^- is incident at the center of strip 5.

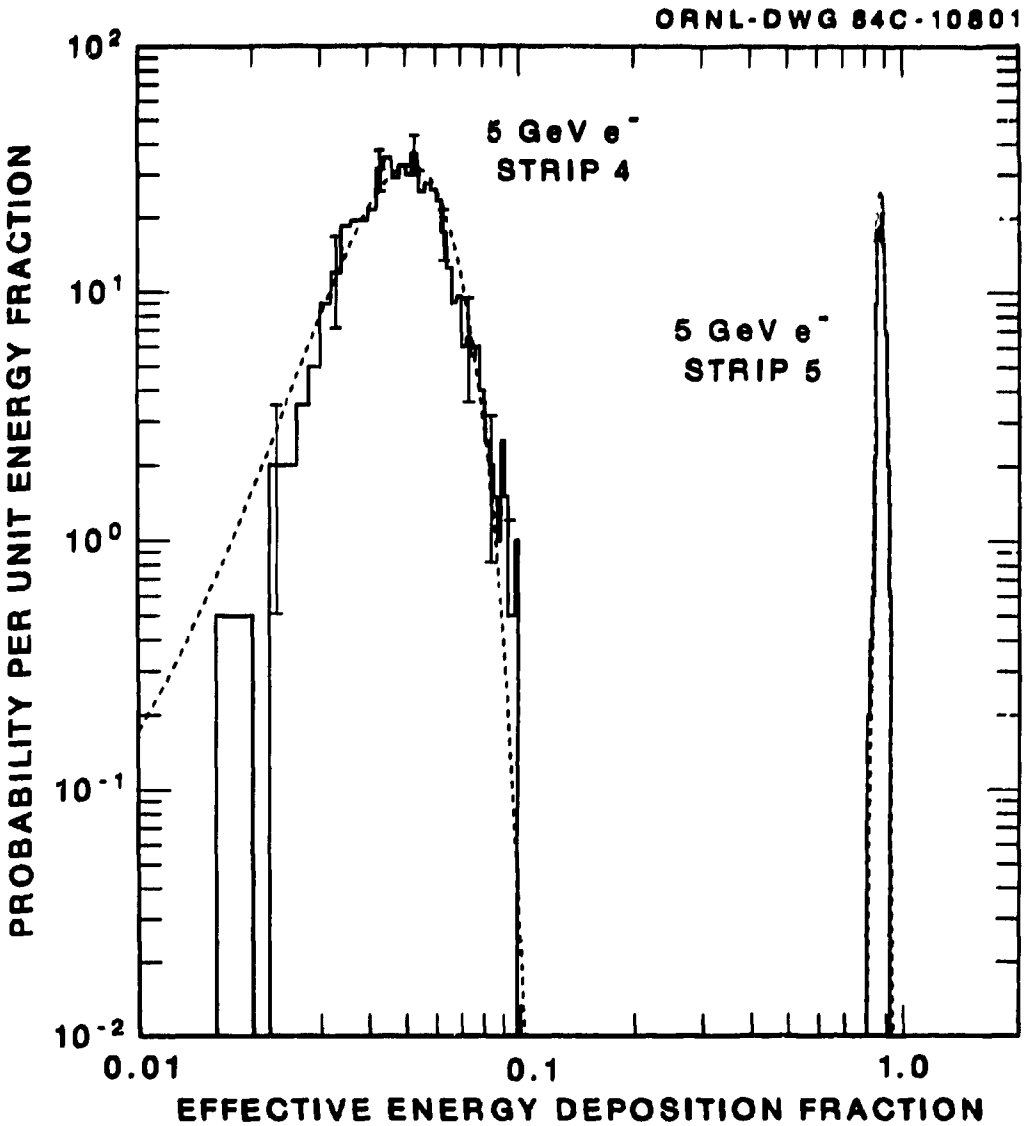

Fig. 14. Probability per unit energy fraction vs. effective energy deposition fraction for broad strips 4 and 5 when 5-GeV e^- is incident at the center of strip 5.

For any value of y_0 (omitted), the average fractions and standard deviations are

$$\bar{F}_j = \sum_{n=1}^{N} F_{nj}/N \ , \tag{3}$$

$$\sigma_{Fj} = \left[\sum_{n=1}^{N} (F_{nj} - \bar{F}_j)^2/(N-1) \right]^{1/2} , \tag{4}$$

where N is the total number of colliding histories. The general shapes of the spectra are very nearly the same for all incident energies, although the pion averages and all sigmas vary some with energy. The electron average fractions are very nearly independent of E_0. This is a result of the fact that the e^- cascades are nearly all contained within the calorimeter core, whereas the π^- cascades are not. Pion spectra for strips 1-3 are more or less decreasing exponentials, not Gaussians; the electron spectra are somewhat in-between.

For center incidence ($y_0 = 0.0$), the π^- spectra for F_{jn} in strip 5 typically show a peak near $F_5 \geq 0.96$, indicating that a small fraction of the cascades (~5%), those in which the primary pion usually collides in the lucite near the middle or the back of the calorimeter and deposits energy near the minimum, are very nearly contained entirely within the impact strip. These cascades would be difficult to distinguish from those of the straight-through pions, but elimination of them would not much affect the moment calculations. (Since all energy is assumed deposited at the center of each strip, the center strip does not contribute, and both first and second moments are zero, if $F_5 = 1.0$.) A corresponding small peak in Fig. 13 indicating some histories with $F_4 = 0.0$ has been omitted. Spectra for the π^- subset look much like those for all π^-, except the peak for $F_5 \geq 0.96$ is missing.

The most noteworthy point about Figs. 12-13 is the fact that as little as 10% or less of the total pion energy can be deposited in strip 5, with a maximum of 55% in one or the other of the strips on either side (4 or 6). The maximum fraction for strips 3 or 7 was about 30%, with a maximum of about 20% for strips 1-2 and 8-9. For e^-, the maximum fractions are about 1%, 2%, 3% and 10% for strips 1, 2, 3, and 4. Many e^- and some π^- do not contribute to the outer strips at all. Again, the spectra of energy fractions in each strip may be greatly altered if y_0 is unequal to zero. Hence, it is not clear that the strip first entered can be determined from the condition of maximum energy deposition, if the particle is a pion. This fact is important when trying to compare experimental values of the first or second lateral moments of the fractional energy distributions with calculations.

The values of $\langle \bar{F}_j(y_0) \rangle$, where the brackets indicate averages over y_0, are shown in Fig. 15, with estimated resolutions for uniform and calculated resolutions for center incidence in Fig. 16a for e^- and Fig. 16b for π^-. Values of $\bar{F}_j$ for center incidence are given in Table 4; (strips 1 and 9 were averaged, etc.).

Some discrimination appears possible in the six outlying strips, which have 10 or 20 times less average and maximum fractional depositions for e^-. For center incidence, the average percent of energy deposited in strips 4 or 6 is only 5% for e^- and 12-14% for π^-. The fractional discrimination in the center strip looks good for center incidence, since all e^- are restricted to a

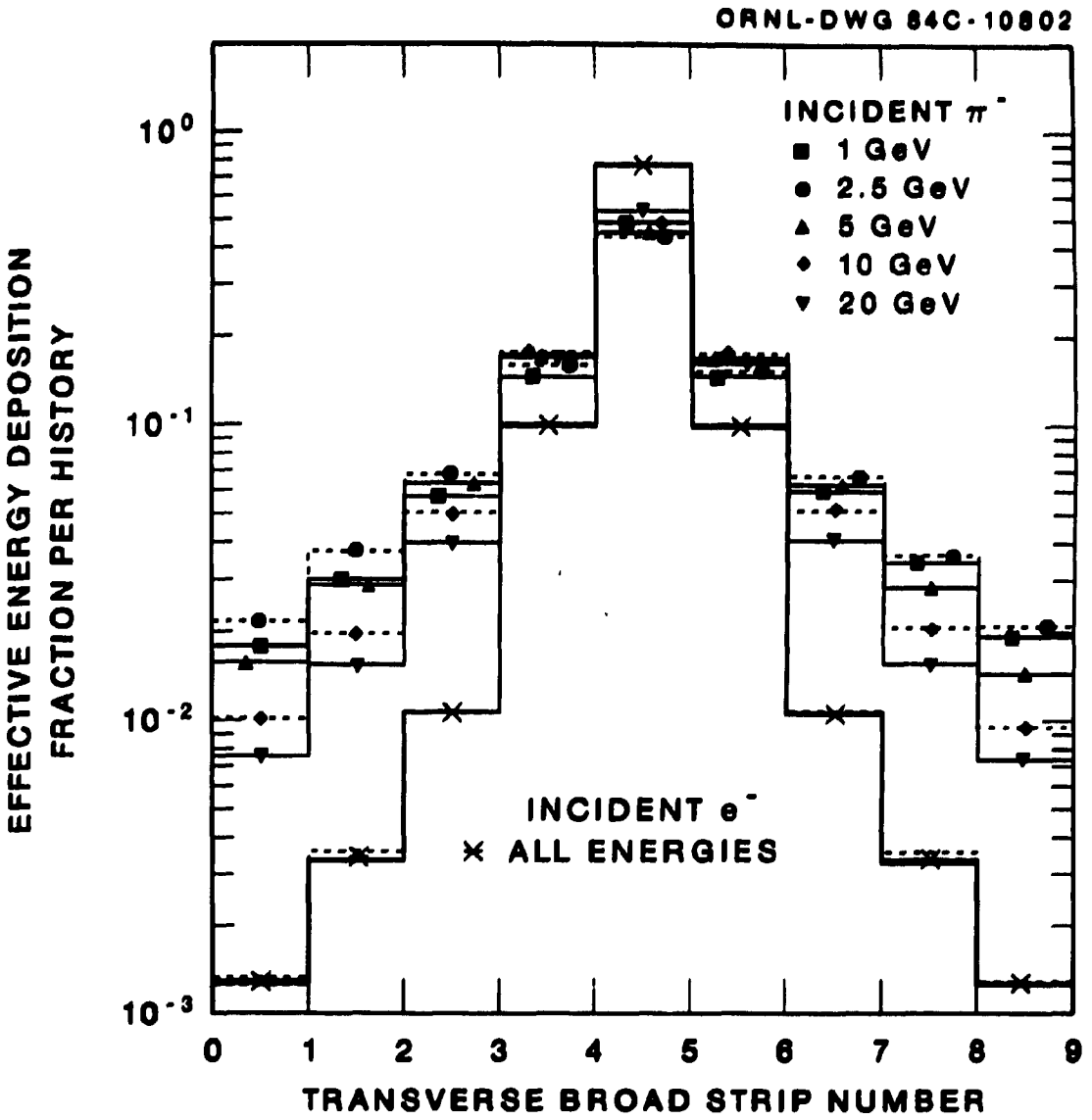

Fig. 15. Fractional energy deposition averaged over point of impact in broad strip 5 vs. broad strip number.

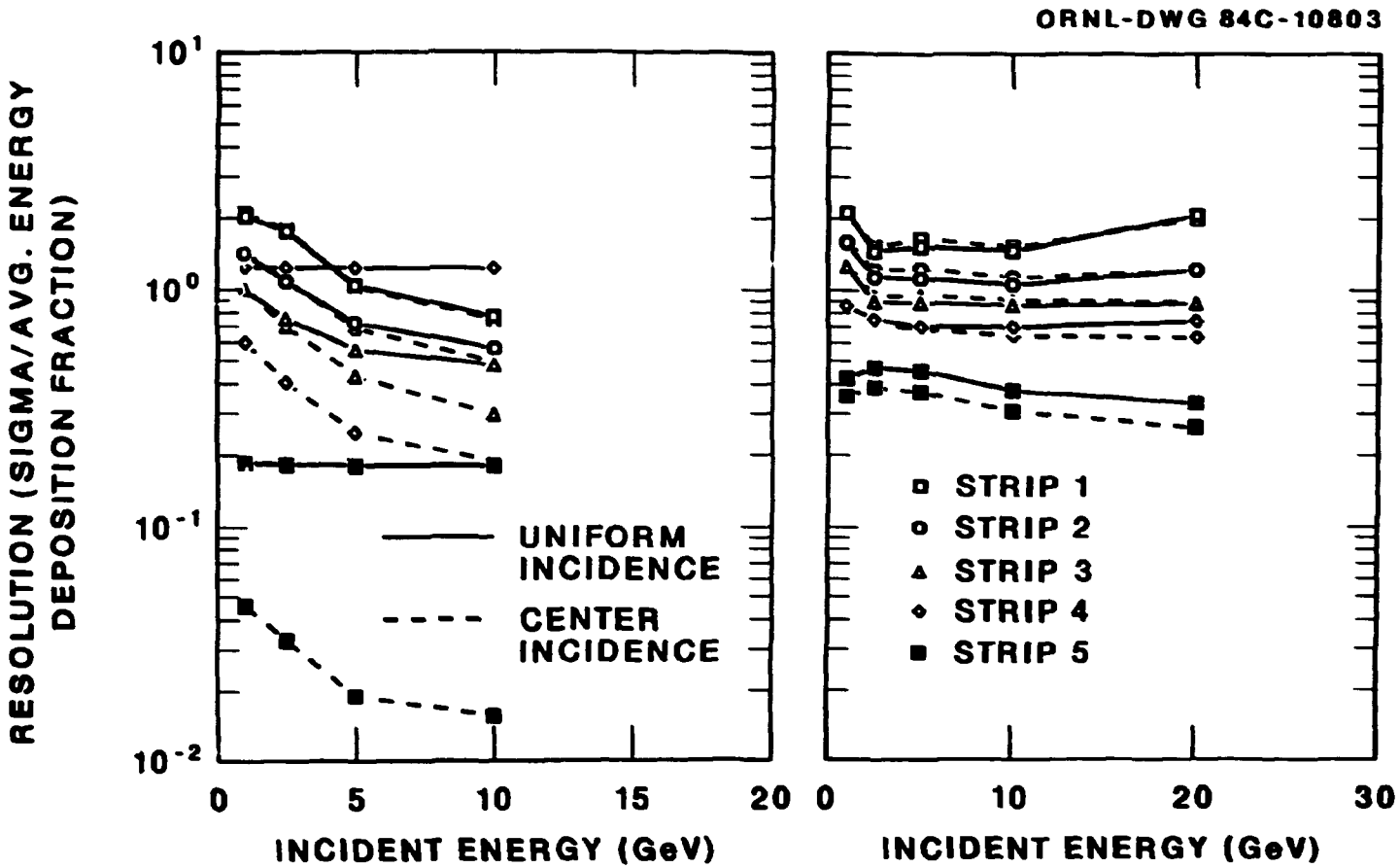

Fig. 16. Resolution for average fractional energy deposition for incident a) e^-, and b) π^-. (Figure 16a is on the left and Fig. 16b is on the right.)

Table 4

Average Percent of Total Energy Deposition in Broad Transverse Strips for Center Incidence

E_0 (GeV)	Strip 1 (%)	Strip 2 (%)	Strip 3 (%)	Strip 4 (%)	Strip 5 (%)
			Incident π^-		
1.0	1.88	3.11	5.51	11.96	55.07
2.5	2.03	3.43	6.15	13.13	50.50
5.0	1.42	2.59	5.67	13.70	53.22
10.0	0.95	1.86	4.57	14.10	57.03
20.0	0.71	1.51	3.66	12.88	62.36
			Incident e^-		
1.0	0.12	0.31	0.97	5.09	87.00
2.0	0.13	0.34	0.99	5.10	86.89
5.0	0.12	0.32	0.97	5.14	86.88
10.0	0.12	0.32	0.97	5.11	86.94
			Incident π^- Subset		
1.0	1.91	3.29	6.03	13.2	51.2
2.5	1.41	2.74	6.12	16.6	46.2
5.0	0.69	1.68	4.39	16.0	54.4
10.0	0.34	0.85	2.71	11.7	68.8

maximum range of about 0.8 to 0.96 (at 1 GeV) contrasted with about 0.01 to 1.0 for π^-. However, the assumption of uniform incidence in the center strip will broaden the e^- ranges to about 0.40 to 0.96, so only about half of the total range is actually left exclusively to π^-. To use this discriminant, one must be certain which strip is first entered.

The first lateral moment, or y-bar, for history n, is

$$y_{bar,n}(y_o) = \sum_{j=1}^{9} F_{nj}(y_o) y_j \ , \tag{5}$$

where y_j is defined to be the distance from the center of strip 5 to the center of strip j, regardless of the value of y_o, which would not be known experimentally. The value of y-bar is thus independent of the fraction of energy in strip 5, except insofar as the sum of the fractions is one. However, the values of y-bar are fairly sensitive to the number of broad strips used; i.e., the outlying strips do contribute, even if the relatively small average fractions are used. If the average y-bar is

$$Y(y_o) = \sum_{n=1}^{N} y_{bar,n}(y_o)/N = \sum_{j=1}^{9} \bar{F}_j(y_o) y_j \ , \tag{6}$$

then the average over y_o, $\langle Y(y_o) \rangle$, is less than 0.05 cm, as is Y for $y_o = 0.0$. Graphs of $|Y|$ versus E_D show that the average y-bar is most nearly zero near the average energy deposition, $\bar{E}_D$. For the relatively high-energy π^- subsets, $|Y|$ is less than 0.1 cm.

The spectra of individual history y-bars are shown in Fig. 17a and 17b for 5-GeV π^- and e^- (center incidence), with Gaussians drawn using

$$\sigma_{y-bar} = \left[\sum_{n=1}^{N} (y_{bar,n} - Y)^2/(N-1) \right]^{1/2} . \tag{7}$$

For center incidence, all e^- y-bar values are within $\pm$ 2 cm; the percentages of π^- with y-bars within these limits are 45% at 1 GeV, 49% at 25 GeV, 57% at 5 GeV, 31% at 10 GeV, and 21% at 20 GeV. Values of the $\sigma_{y\text{-bar}}$ versus E_o are shown in Fig. 18. These will be somewhat broadened if variation with y_o is taken into account, particularly for e^-. For uniform incidence over the center strip, some individual absolute vaues of y-bar may be increased by more than 3 cm, if the point of impact in strip 5 is moved to either edge of the strip. Very large absolute values of y-bar can generally be attributed to pions.

Second lateral moments can be calculated for individual histories, with σ_{yn} and its average given by

$$\sigma_{yn} = \left[\sum_{j=1}^{9} F_{nj}(y_j - y_{bar,n})^2 \right]^{1/2} , \tag{8}$$

$$\bar{\sigma}_y = \sum_{n=1}^{N} \sigma_{yn}/N \ . \tag{9}$$

Spectra of σ_{yn} for center incidence are shown in Figs. 19a and 19b for 5-GeV π^- and e^-. For e^-, all σ_{yn} are less than 6 cm; for π^-, 64% to 82% lie outside these limits. Average values are shown with their standard deviations in Fig. 20 as functions of E_o. The spectra of σ_{yn} are not changed very much if $y_{bar,n}$ in Eq. (8) is replaced by zero. The only difference is a reduction in the slight peak near $\sigma_y = 0.0$. This peak is attributed to the particles with $F_5 \geq 0.96$, as shown in Fig. 13. No dependence of $\bar{\sigma}_y$ on energy deposition (for a fixed E_o) was found. Again, the σ_{yn} distributions will be broadened if uniform incidence over y_o is taken into account. Large values of σ_y may serve to discriminate some π^- from e^-.

Figures 18 and 20 also show average $\sigma_{y\text{-bar}}$ and $\bar{\sigma}_y$ for the π^- subset; they are not appreciably different from those for pions with smaller energy depositions.

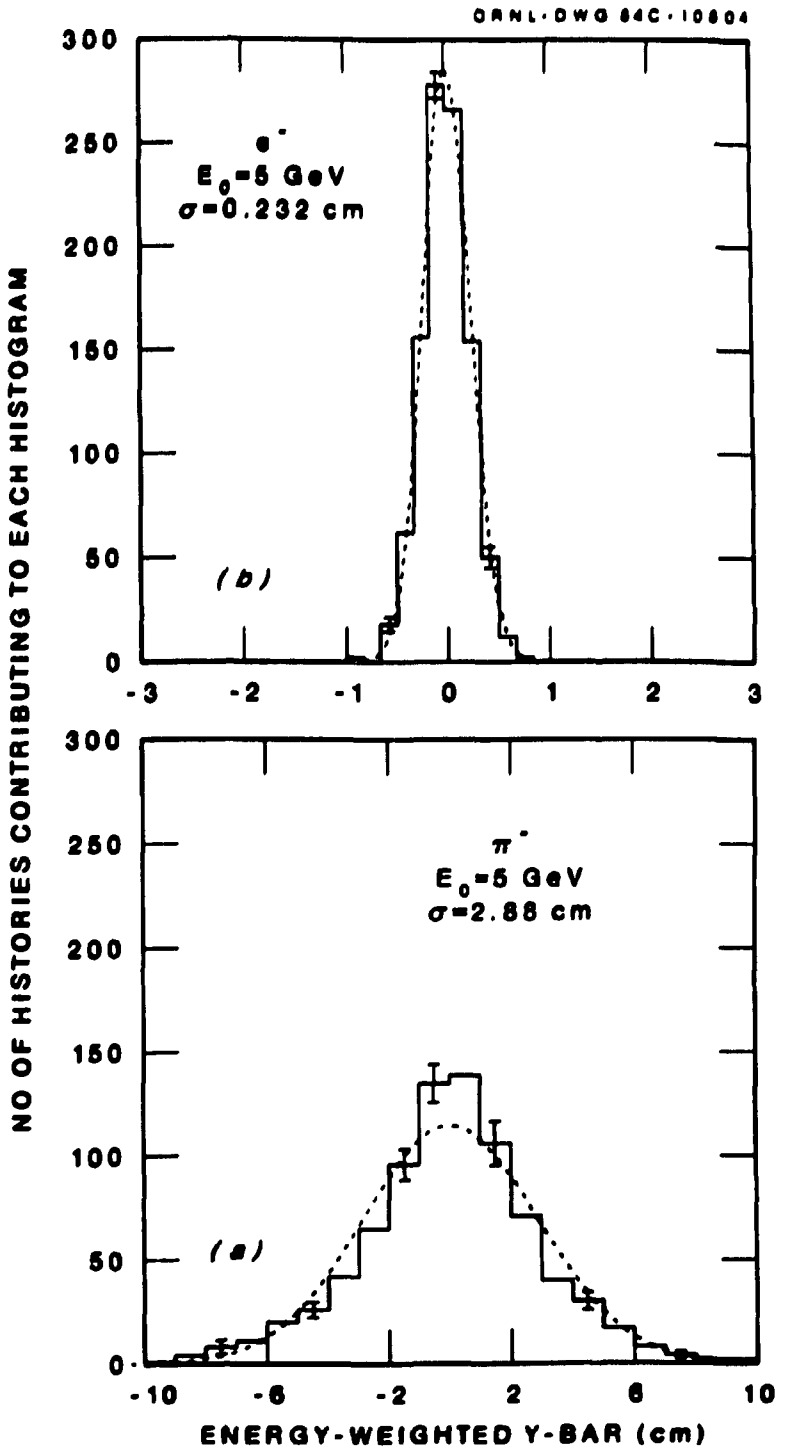

Fig. 17. Fractional-energy-weighted y-bar ($\bar{y}_n$) spectra for 5-GeV incident e^- and π^-.

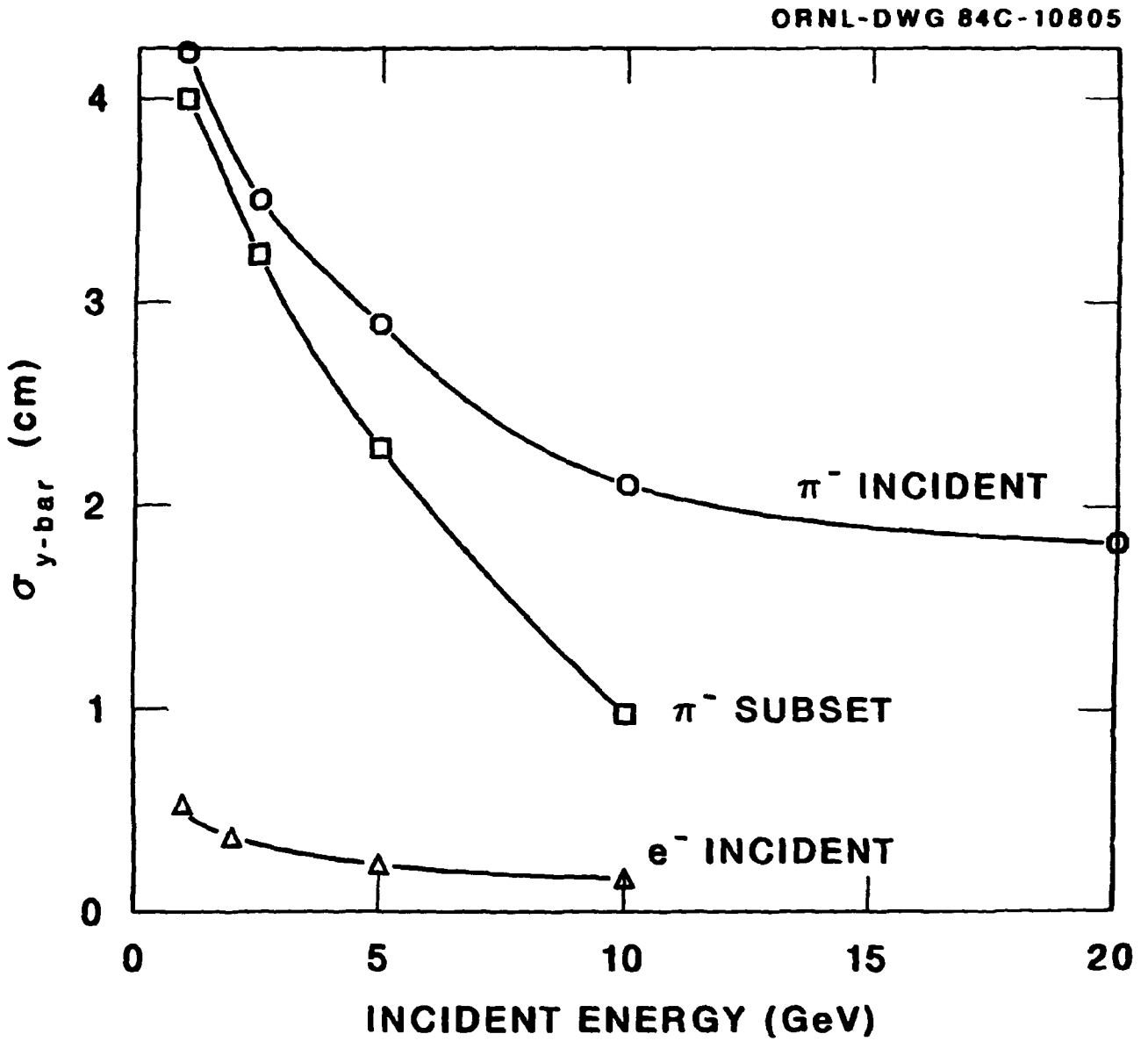

Fig. 18. Standard deviations of y-bar distributions vs. incident energy for π^- and e^- incident at the center of strip 5.

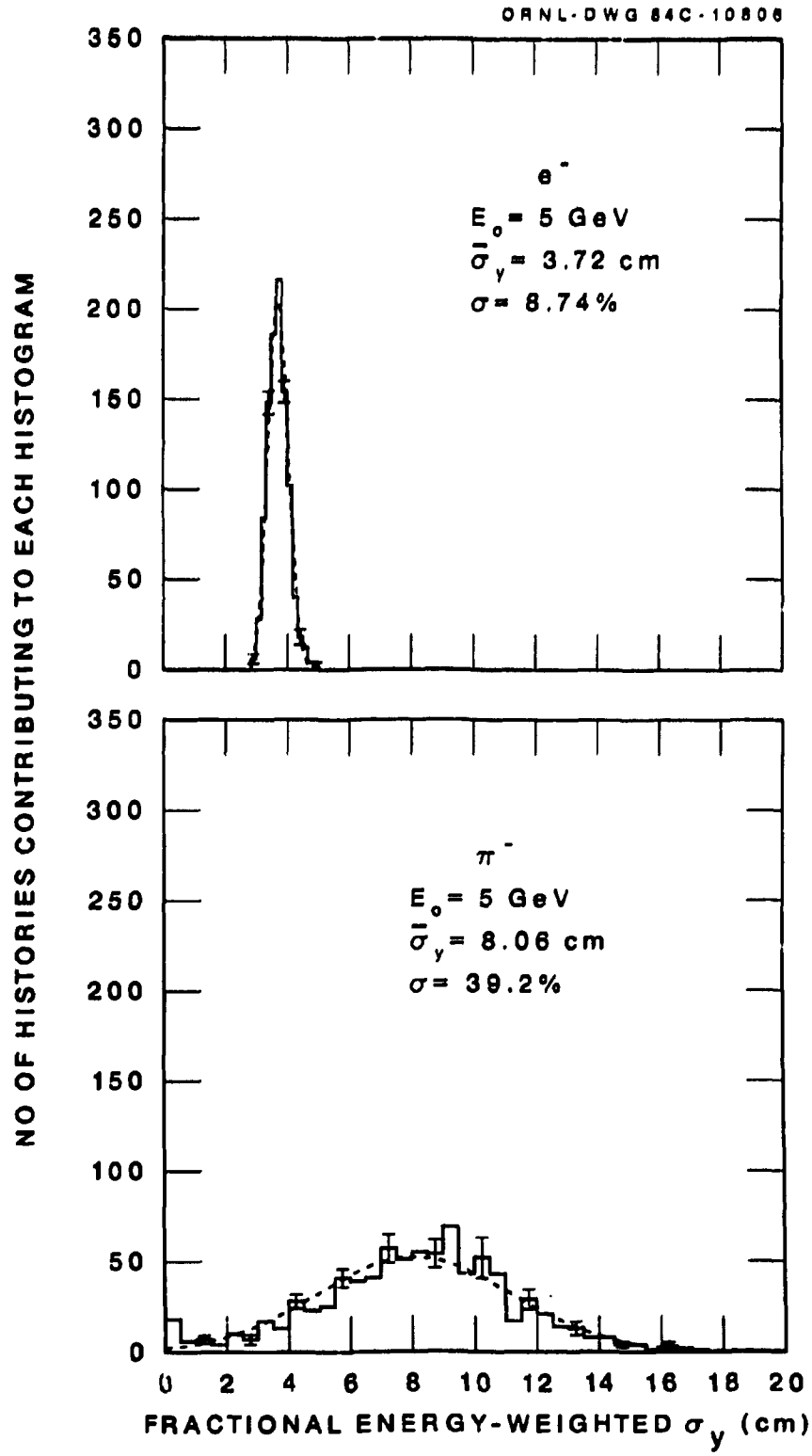

Fig. 19. Spectra of fractional-energy-weighted σ_y's for a) 5-GeV π^-, b) 5-GeV e^- incident at the center of strip 5.

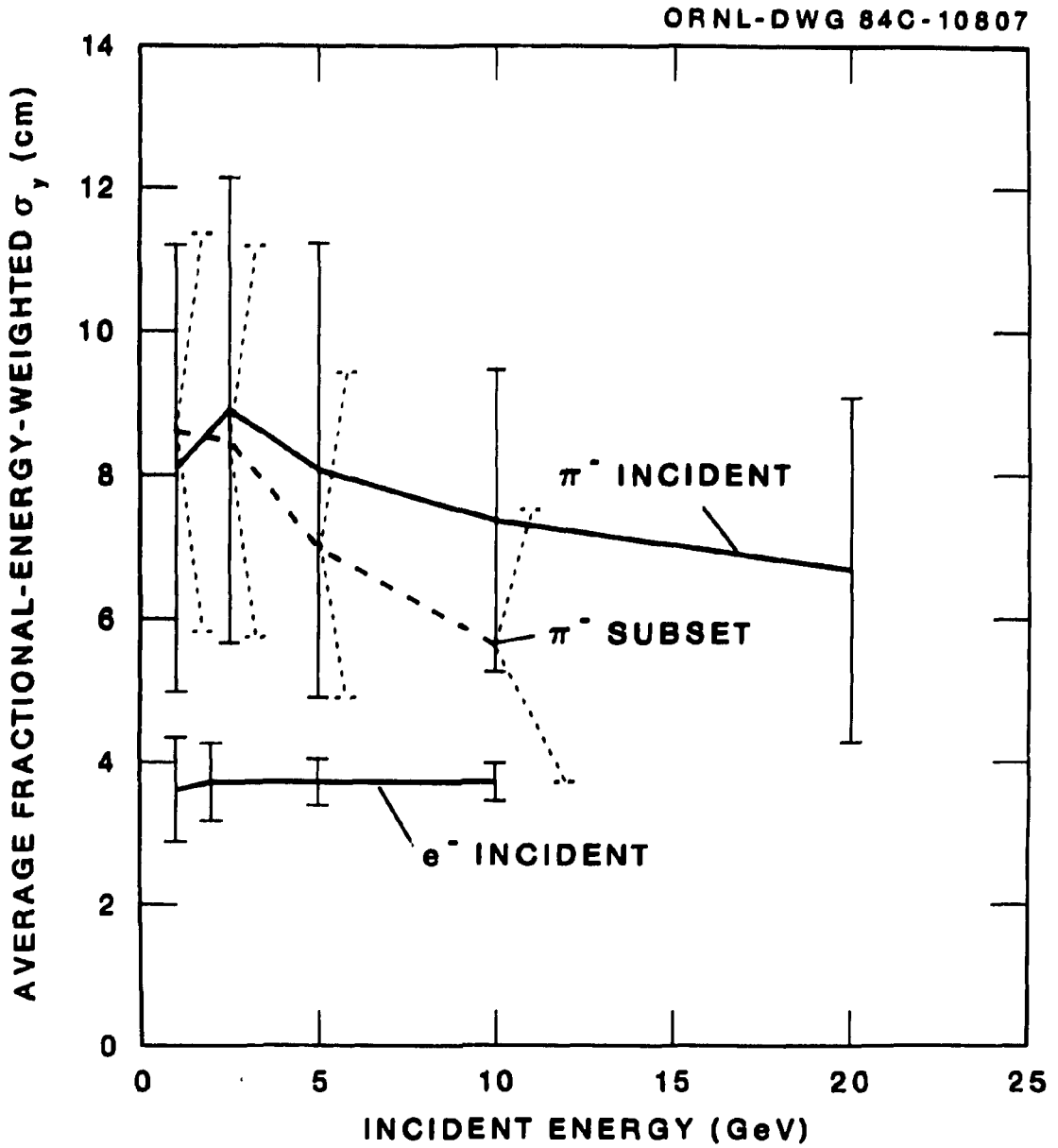

Fig. 20. Average fractional-energy-weighted σ_y, e.g., Fig. 19, vs. incident energy. The error bars are the standard deviations of the σ_y distributions.

VII. LONGITUDINAL DISCRIMINANTS

A first glance at the average longitudinal energy distribution shows a much higher energy deposition at the back of the calorimeter for high-energy π^-, but standard deviations are large. Table 5 shows the percent of colliding particles with energy deposition in lucite plate 60 less than 4, 8, and 16 MeV, respectively, for π^-, e^-, and π^-_{subset}. The average energy deposited and standard deviations for each limit are also given. The spectra are exponential; the maximum energies, $E_{60,max}$, for the data sets considered are also shown in Table 5. For 10 GeV e^-, only about 5% deposit energy between 8 and 16 MeV, with a single e^- history depositing 30 MeV. The remainder of the e^- deposit less than 8 MeV here. About 5% of the 1-GeV π^- deposit energy between 8 and 50 MeV, with percentages up to 80% for higher energy π^-; a few π^- deposit energies up to 368 MeV in plate 60. The test for $E_D > 8$ MeV will not help much for the π^- subset, but otherwise will screen out from 40 to 80% of the π^- at $E_0 \geq 5$ GeV.

A second glance at Fig. 4 suggests measuring the energy difference between three successive sections of the calorimeter (not the same as the orientations previously discussed). The three plate sets are the first 21, second 21, and last 18 lucite plates. These could be obtained if the light output for the 20-plate sets of each orientation could be divided into light output from sets of 7, 7, and 6 plates and then re-combined.

Spectra for any of these energy differences show differences greater than zero for 70 to 100% of the e^-, and differences greater than zero for 30 to 50% of the π^-, but no clear cut separation of particles. In Fig. 21 the fractions of histories with energy differences greater than zero are shown as functions of E_0 for each permutation of plate set differences. The π^- fraction should be multiplied by the probability, P_{coll}, that a pion will collide (P_{coll} is the number of histories shown in Fig. 8, divided by 1000) to get the total probability of an energy difference greater than zero. Assuming equal probabilities of π^- or e^- in the initial beam, the ratio of the e^- fraction to the product of the π^- fraction with P_{coll} for any permutation is a rough measure of the relative probability of e^- to π^- at the selected E_0's, if the energy difference is positive. If it is negative, use the fractions < 0.0 ($= 1.0 -$ fraction > 0.0).

If one simply divides the calorimeter into two halves and finds the difference of the energy deposition in the front minus that in the back, and uses the fact that the spectra of e^- differences lie within the maximum π^- energy difference and zero, then the conservative method above is accurate. At $E_0 = 1$ GeV, a π^- is $0.71/P_{coll}$ times as probable as an e^- if the energy difference is positive, and an e^- is only $0.0021/P_{coll}$ times as probable as a π^-, if it is negative. These percentages are taken from Table 6, which also gives the average energy differences and standard deviations. In the last two columns, the average ratios of energy deposited in the back to energy deposited in the front are given, with standard deviations. These average ratios are 8 to 19 times as great for π^- as for e^- as E_0 increases from 1 to 10 GeV, but the spectra are not Gaussian.

A variant discriminant using the shape of the longitudinal distribution is to assume measurements of the energy deposition in a plate near the maximum for e^-, e.g., plate 15, and also in plate 60, and to take the difference. Computed spectra of these differences show positive values for virtually all electrons studied and for about 50 to 60% of all pions. Thus, any negative value not very near zero can be attributed to a pion. This is not a very helpful discriminant for the π^- subsets, which show few negative values.

The percent of particles with $E_{15} - E_{60}$ greater than zero, as well as the average values of this energy difference and standard deviations, are given in Table 6.

Table 5

Percent of Colliding Particles with Energy Deposition in Lucite Plate 60 Less Than the Specified E_{max}, Average Energy Deposition by the Fraction of Particles with Energy Less Than E_{max}, and the Standard Deviation

	E_{max} = 4 MeV			E_{max} = 8 MeV			E_{max} = 16 MeV			Upper Limit
E_o (GeV)	% $<E_{max}$	$\bar{E}_{60}$ (MeV)	Std. Dev. (MeV)	% $<E_{max}$	$\bar{E}_{60}$ (MeV)	Std. Dev. (MeV)	% $<E_{max}$	$\bar{E}_{60}$ (MeV)	Std. Dev. (MeV)	$E_{60,max}$ (MeV)
					Incident π^-					
1.0	90.1	0.39	1.02	95.4	6.79	1.58	98.3	1.00	2.45	83
2.5	76.8	0.86	1.40	85.8	1.37	2.00	91.0	1.93	3.10	116
5.0	44.9	1.51	1.60	59.9	2.61	2.42	76.0	4.46	4.32	140
10.0	21.4	1.83	1.69	38.4	3.64	2.55	58.4	6.42	4.62	203
20.0	7.5	1.81	1.66	19.2	4.20	2.44	33.8	7.47	4.46	368
					Incident e^-					
1.0	99.6	0.08	0.36	100	0.10	0.48	100.0	0.10	0.48	6
2.0	99.6	0.09	0.36	100	0.11	0.52	100.0	0.11	0.52	7
5.0	95.6	0.34	0.72	99.6	0.55	1.26	100.0	0.59	1.44	13
10.0	84.8	0.75	1.02	94.8	1.28	1.85	99.8	1.74	2.76	30
					Incident π^- Subset					
1.0	87.4	0.16	0.61	95.4	0.63	1.70	97.5	8.67	2.32	83
2.5	76.7	0.41	0.92	90.4	1.17	2.00	95.9	1.69	2.93	62
5.0	65.4	0.81	0.98	84.6	1.93	2.35	96.2	3.17	1.30	21
10.0	60.0	0.59	1.31	80.0	1.73	2.26	90.0	3.13	4.88	24

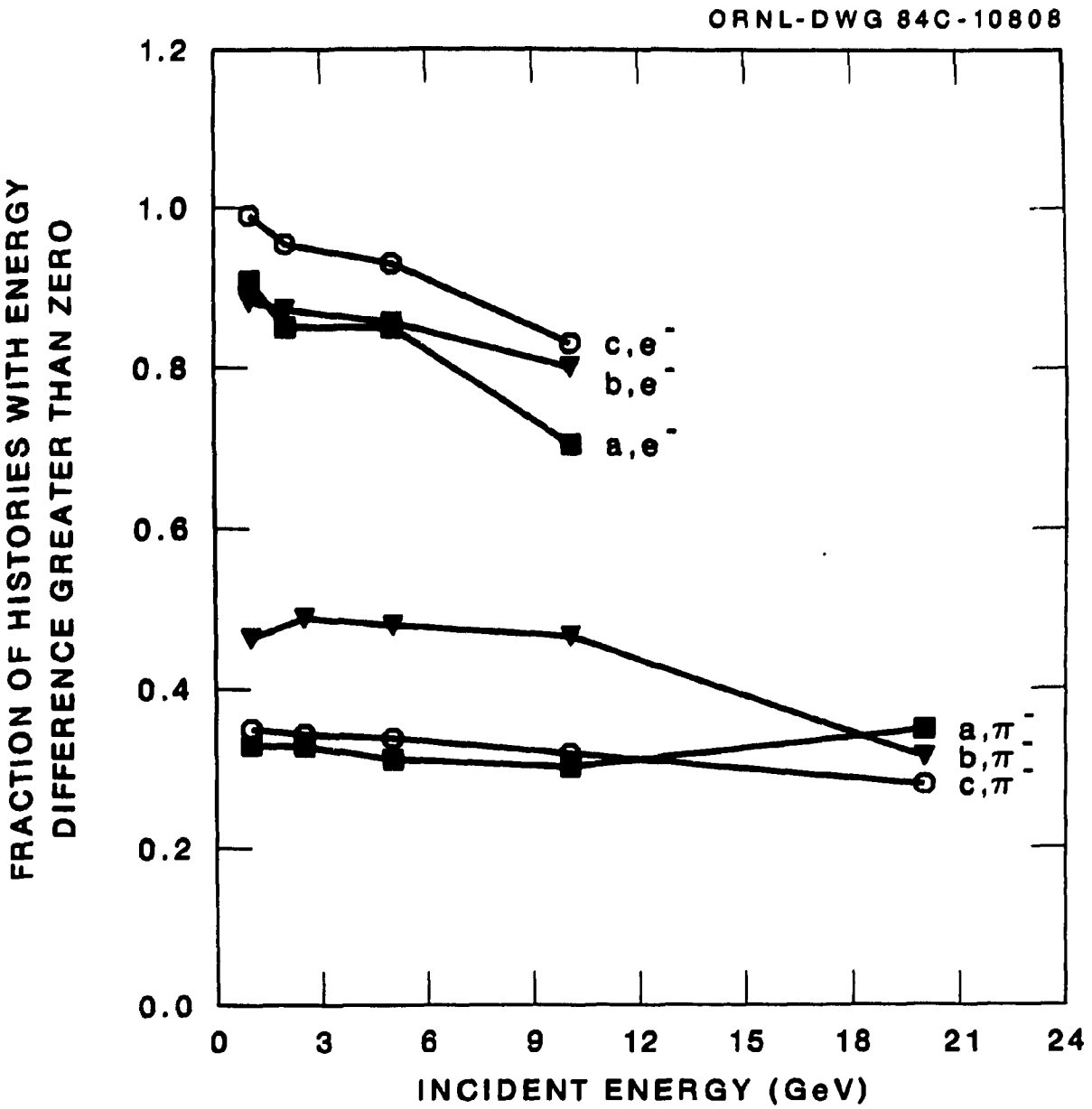

Fig. 21. Relative number of particles with energy differences between lucite plate sets greater than zero: a) first 21 plates minus second 21 plates, b) first 21 plates minus last 18 plates, and c) second 21 plates minus last 18 plates.

Table 6

Percent of Colliding Particles with Energy Deposition Differences Greater Than Zero, Average Values of Energy Differences, and Standard Deviations
a) Plate 15 − Plate 60
b) (Plates 1 to 30) − (Plates 31 to 60)

Note: Last two columns give average ratio of energy deposition in back half of calorimeter to that in front half, with standard deviations.

	a			b				
E_o (GeV)	% $E_{Diff.}>0$	$\bar{E}_{15}-\bar{E}_{60}$ (MeV)	Std. Dev. (MeV)	% $E_{Diff.}>0$	$\bar{E}_{Front}-\bar{E}_{Back}$ (MeV)	Std. Dev. (MeV)	$<E_{Back}/E_{Front}>$	Std. Dev.
				Incident π^-				
1.0	83	5.2	12.5	71	104	156	0.73	0.88
2.5	71	6.6	21.9	57	86	314	1.4	1.7
5.0	54	4.1	29.6	45	-37	527	2.4	2.7
10.0	46	3.7	50.9	38	-155	903	3.0	3.9
20.0	39	-3.9	88.4	33	-555	1631	4.2	6.2
				Incident e^-				
1.0	99.4	17	10	99.4	321	65	0.098	0.25
2.0	100.0	34	14	99.8	651	86	0.076	0.086
5.0	99.8	87	27	99.2	1467	289	0.14	0.20
10.0	100.0	167	44	100.0	2723	504	0.16	0.10
				Incident π^- Subset				
1.0	86	7	14	66	116	203	0.93	1.06
2.5	79	19	26	62	156	577	2.0	2.7
5.0	92	36	35	73	507	796	1.0	1.5
10.0	80	101	85	80	1116	1974	1.2	1.8

SUMMARY

All calculations assume normal incidence and energy deposition in nine broad transverse strips symmetric about the strip first entered.

The calorimeter is thin for π^- ($\leq$1.8 collision mean-free paths) but thick for e^- ($\sim$20 radiation lengths). Hence, the calculated resolutions for normally incident 1- to 10-GeV e^- are very good (<6%). The resolutions for 1- to 20-GeV π^- are very large (31-61%), and hadron-lepton discrimination at a measured energy deposition is very problematic. Virtually any pion with initial energy greater than or equal to that minimally necessary for an electron could produce the measured energy deposition.

The best discriminants appear to be longitudinal, but are not much better than about 50%, with the exception of back/front ratios. Average ratios of energy deposition in the back half of the calorimeter to that in the front half are ten to twenty times larger for π^- than for e^-, even at $E_0 < 5$ GeV. At initial energies less than 5 GeV, measurements of energy deposition in the last lucite plate, or plates, are of little value.

Transverse discriminants include the lateral energy depositions and the lateral fractional energy depositions in each strip, with first and second moments. To use these, one should know the strip first entered.

The typical energy depositions in each transverse strip are valid even if "strip 5" is off-center and if fewer than nine strips are used. Averages were computed for uniform incidence and were shown with estimated resolutions in Figs. 6 and 7. The lateral energy distribution is definitely not as broad for e^- as for π^-, and the e^- ratio, $\bar{E}_{Dj}/E_0$, is a constant for each strip j, as well as for the sum over all strips. However, the resolutions are large.

Spectra of the individual particle energy deposition fractions do depend somewhat upon the use of nine strips. For uniform incidence, fractions of the total energy deposition that are less than 40%, or greater than 96%, in the "center" strip, are almost certainly due to pions. Electron fractions in the off-center strips are generally 5 to 10 times smaller than those for pions.

For center incidence in strip 5, first moments, or y-bars, greater than about $\pm$ 2 cm are attributable to pions. Similarly, a σ_y greater than 6 cm indicates a pion. However, the extensions of these y-bar or σ_y limits when uniform incidence is assumed are not given here. Also, four strips on either side of the center strip were used to obtain these results; fewer strips would give smaller moments.

If a prior determination of initial energy is made, a pion subset that is small at incident energies greater than 1 GeV (1.1% at 10 GeV; 3.1% at 5 GeV; 9% at 25 GeV; 41% at 1 GeV) remains which could produce energy depositions in the same range as those for e^-. The transverse statistics for these pions are similar to those for other pions. Longitudinal discriminants are not of much help for the subsets, with the exception of back/front ratios.

REFERENCES

1. T. Jensen, J. D. Amburgey, and T. A. Gabriel, "Hadronic- and Electromagnetic-Cascade Discrimination in a Thin Lead-Argonne Calorimeter," *Nucl. Instr. Methods* **143**, 429 (1977).
2. B. M. Bleichert, C. Grupen, and D. Mattern, "Particle Identification in an Electron/Hadron Calorimeter," *Nucl. Instr. Methods* **212**, 145 (1983).
3. A. S. Vovenko et al., "Energy Resolution and Structure of a Calorimeter," *Nucl. Instr. Methods* **212**, 155 (1983).
4. K. C. Chandler and T. W. Armstrong, "Operating Instructions for the High-Energy Nucleon-Meson Transport Code, HETC," ORNL-4744, Oak Ridge National Laboratory (1972).
5. T. W. Armstrong et al., "Monte Carlo Calculations of High-Energy Nucleon-Meson Cascades and Comparison with Experiment," *Nucl. Sci. Eng.* **49**, 82 (1972).
6. T. A. Gabriel, J. D. Amburgey, and B. L. Bishop, "CALOR: A Monte Carlo Program for the Design and Analysis of Calorimeter Systems," ORNL/TM-5619, Oak Ridge National Laboratory (1977).
7. T. A. Gabriel et al, "A Monte Carlo Simulation of an Actual Segmented Calorimeter: A Study of Calorimeter Performance at High Energies," *Nucl. Instr. Methods* **195**, 461 (1982).
8. T. A. Gabriel and B. L. Bishop, "Calculated Response of a Total Liquid Argon Calorimeter," *Nucl. Instr. Methods* **169**, 427 (1980).
9. T. A. Gabriel and B. L. Bishop, "The Response of a Uranium-Plastic Calorimeter to Low GeV ($\leq$10 GeV) Protons," *Nucl. Instr. Methods* **164**, 609 (1979).
10. T. A. Gabriel and W. Schmidt, "Calculated Performance of Iron-Argon and Iron-Plastic Calorimeters for Incident Hadron With Energies of 5 to 75 GeV," *Nucl. Instr. Methods* **134**, 271 (1976).
11. R. T. Santoro, J. D. Amburgey, and T. A. Gabriel, "The Calculated Response of a Liquid Scintillator, Total-Absorption Hadron Calorimeter," *Nucl. Instr. Methods* **134**, 87 (1976).
12. T. A. Gabriel, R. T. Santoro, and J. Barish, "A Calculational Method for Predicting Particle Spectra from High-Energy Nucleon and Pion Collisions ($\geq$3 GeV) With Protons," Oak Ridge National Laboratory, ORNL/TM-4585 (1970).
13. H. W. Bertini, M. B. Guthrie and A. H. Culkowski, "Phenomenologically Determined Isobar Distributions for Nucleon-Nucleon and Pion-Nucleon Reactions Below 3 GeV," Oak Ridge National Laboratory, ORNL/TM-3132 (1970).
14. R. L. Ford and W. R. Nelson, "The EGS Code System: Computer Program for the Monte Carlo Simulation of Electromagnetic Cascade Showers (Version 3)," SLAC-210, Stanford Linear Accelerator Center (1978).

INTERNAL DISTRIBUTION

1–3. L. S. Abbott
4–8. F. S. Alsmiller
9–13. R. G. Alsmiller, Jr.
14. D. E. Bartine
15. B. L. Bishop
16–20. EP&M Reports Office
21–25. T. A. Gabriel
26. R. A. Lillie
27. F. C. Maienschein
28. R. W. Peelle
29. RSIC
30. R. T. Santoro
31. A. Zucker
32. P. W. Dickson, Jr. (Co...
33. G. H. Golub (Consultan...
34. H. J. C. Kouts (Consult...
35. D. Steiner (Consultant)
36–37. Central Research Library
38. ORNL Y-12 Technical Library Document Reference Section
39–40. Laboratory Records
41. ORNL Patent Office
42. Laboratory Records - RC

EXTERNAL DISTRIBUTION

43. Office of Assistant Manager for Energy Research & Development, DOE-ORO, Oak Ridge, TN 37830

44. Argonne National Laboratory, Library Services Department, 302-CE125, 9700 S. Cass Avenue, Argonne, IL 60439

45. T. W. Armstrong, Science Applications, Inc., PO Box 2807, La Jolla, CA 92038

46. Miguel Awschalom, National Accelerator Laboratory, PO Box 500, Batavia, IL 60510

47. V. S. Barashenkov, Laboratory of Theoretical Physics, Joint Institute for Nuclear Research, Head Post Office, PO Box 79, Moscow, USSR

48. Dr. Gerald W. Bennett, Brookhaven National Laboratory, Upton, NY 11973

49. Dr. Elliott Bloom, Stanford Linear Accelerator Center, PO Box 4349, Stanford, CA 94305

50. Brookhaven National Laboratory, Attention: Research Library, Upton, NY 11973

51. Dr. Bruce Brown, Fermi National Accelerator Laboratory, PO Box 500, Batavia, IL 60510

52. Dr. David O. Caldwell, Department of Physics, University of California at Santa Barbara, Santa Barbara, CA 93106

53. Stanley B. Curtis, Lawrence Radiation Laboratory, Bldg. 29, Room 213, Berkeley, CA 94720

54. Herbert Destaebler, Stanford Linear Accelerator Center, Stanford University, Stanford, CA 94305

55. R. D. Edge, Physics Department, University of South Carolina, Columbia, SC 29208

56. Dr. R. Eisenstein, Department of Physics, University of Illinois, Urbana, IL 61801

57. Dr. Chris Fabjan, CERN, Geneva 23, Switzerland

58. Dr. G. Feldman, Stanford Linear Accelerator Center, Stanford University, Stanford, CA 94305

59. Dr. W. T. Ford, Experiment lA-Lab C, Fermi National Accelerator Laboratory, PO Box 500, Batavia, IL 60510

60. Dr. E. Fowler, Department of Physics, Purdue University, West Lafayette, IN 47907

61. E. Freytag, Deutsches Elektronen-Synchrotron, DESY, 2 Hamburg Dr., Flottbek, Notkesteig l, W. Germany

62. Dr. G. T. Gillies, Department of Physics, University of Virginia, Charlottesville, VA 22901

63. Dr. Gary E. Gladding, University of Illinois, Department of Physics, Urbana, IL 61801

64. K. Goebel, Health Physics Group, CERN, 1211 Geneva 23, Switzerland

65. Dr. M. Goodman, Department of Physics, Harvard University, Cambridge, MA 02138

66. Dr. Herman Grunder, Deputy Director, General Sciences, Lawrence Berkeley Laboratory, Bldg. 50A, Room 4119, 1 Cyclotron Rd., Berkeley, CA 94720

67. Frenc Hajnal, Health and Safety Laboratory, U.S. Department of Energy, 376 Hudston St., NY, NY 10014

68. Dr. D. Hitlin, Stanford Linear Accelerator Center, Stanford Univers ty, Stanford, CA 94305

69. M. Hofert, CERN, 1211 Geneva 23, Switzerland

70. Mr. Terrence Jensen, Dept. of Physics and Astronomy, The University of Rochester, Rochester, NY 14627

71. Prof. D. Lal, Tata Institute of Fundamental Research, National Centre of the Government of India for Nuclear Science & Mathematics, Homi Bhabha Rd., Bombay 5, India

72. Lawrence Livermore Laboratory, Technical Information Department, PO box 808, Livermore, CA 94550

73. V. Lebedev, Institute of High Energy Physics, Serpukhov, Moscow Region, USSR

74. Library for Nuclear Science, Massachusetts Institute of Technology at Middleton, Middleton, MA 01949

75. Dr. J. LoSecco, Department of Physics, California Institute of Technology, Pasadena, CA 91125

76. Dr. J. Marks, Accelerator Fusion Research Division, Lawrence Berkeley Laboratory, Bldg. 50, Room 149, 1 Cyclotron Rd., Berkeley, CA 94720

77. Dr. V. S. Narasimham, Tata Institute of Fundamental Research, Bombay 400 005, India

78. W. R. Nelson, Stanford Linear Accelerator Center, Stanford University, PO Box 4349, Stanford, CA 94305

79. Keran O'Brien, Health and Safety Laboratory, U.S. Department of Energy, 376 Hudson St., NY, NY 10014

80. Dr. T. R. Palfrey, Jr., Department of Physics, Purdue University, West Lafayette, IN 47907

81. Dr. Robert Palmer, Brookhaven National Laboratory, Upton, NY 11973

82. Dr. C. W. Peck, Department of Physics, California Institute of Technology, Pasadena, CA 91109

83. J. Ranft, Karl-Marx University, Physics Section, Linnestrasse 5, 701 Leipzig, W. Germany

84. Dr. Lincoln Reed, Division of High Energy and Nuclear Physics, Department of Energy, Washington, DC 20545

85. Dr. C. Rubbia, Lyman Laboratory, Harvard University, Cambridge, MA 02138

86. Dr. W. Schmidt, Institute of Experimental Nuclear Physics, University of Karlsruhe, 75 Karlsruhe, W. Germany

87. The Secretary, Radiation Group, Lab II, CERN, 1211 Geneva 23, Switzerland

88. Dr. Walter Selove, University of Pennsylvania, Department of Physics, Philadelphia, PA 19104

89. B. S. P. Shen, Department of Astronomy, University of Pennsylvania, Philadelphia, PA 19104

90. Dr. M. Shupe, Department of Physics, University of Minnesota, Minneapolis, MN 55455

91. Stanford Linear Accelerator Center, Attention: Library, PO Box 4349, Stanford, CA 94305

92. Dr. Alan Stevens, Physics Department, Brookhaven National Laboratory, Upton, NY 11973

93. G. R. Stevenson, Radiation Protection Group, Lab II, CERN, 1211 Geneva 23, Switzerland

94. Dr. L. Sulak, Department of Physics, University of Michigan, Ann Arbor, MI 48109

95. R. F. Taschek, Los Alamos National Laboratory, P.O. Box 1663, Los Alamos, NM 87544

96. R. Tesch, DESY, Hamburg, Notkesteig 1, W. Germany

97. Ralph H. Thomas, University of California, Lawrence Radiation Laboratory, Health Physics Department, Bldg.72, Berkeley, CA 94720

98. V. D. Toneev, Laboratory of Theoretical Physics, Joint Institute for Nuclear Research, Head Post Office, PO Box 79, Moscow, USSR

99. W. Turchinetz, Massachusetts Institute of Technology, R26-411, Cambridge, MA 02139

100. Dr. W. J. Willis, CERN, Geneva 23, Switzerland

101. Dr. D. Winn, Lyman Laboratory, Harvard University, Cambridge, MA 02138

102. Dr. J. Wilcznski, Nuclear Research Center, Karlsruhe, W. Germany

103. Dr. S. Yellin, Stanford University, Stanford Linear Accelerator Center, P.O. Box 4349, Stanford, CA 94305

104. Dr. B. Zeitnitz, Nuclear Research Center, Karlsruhe, W. Germany

105–131. Technical Information Center